



# Accretion and Uneven Depletion of the Main Asteroid Belt

Rogério Deienno<sup>1</sup> , David Nesvorný<sup>1</sup> , Matthew S. Clement<sup>2</sup> , William F. Bottke<sup>1</sup> , André Izidoro<sup>3</sup> , and Kevin J. Walsh<sup>1</sup>

<sup>1</sup> Solar System Science & Exploration Division, Southwest Research Institute, 1050 Walnut Street, Suite 300, Boulder, CO 80302, USA; [rogerio.deienno@swri.org](mailto:rogerio.deienno@swri.org), [rdeienno@boulder.swri.edu](mailto:rdeienno@boulder.swri.edu)

<sup>2</sup> Johns Hopkins APL, 11100 Johns Hopkins Road, Laurel, MD 20723, USA

<sup>3</sup> Department of Earth, Environmental and Planetary Sciences, MS 126, Rice University, Houston, TX 77005, USA

Received 2023 December 13; revised 2024 March 27; accepted 2024 April 2; published 2024 May 7

## Abstract

The main asteroid belt (MAB) is known to be primarily composed of objects from two distinct taxonomic classes, generically defined here as S- and C-complex. The former probably originated from the inner solar system (interior to Jupiter's orbit), while the latter probably originated from the outer solar system. Following this definition, (4) Vesta, a V-type residing in the inner MAB ( $a < 2.5$  au), is the sole  $D > 500$  km object akin to the S-complex that potentially formed in situ. This provides a useful constraint on the number of  $D > 500$  km bodies that could have formed, or grown, within the primordial MAB. In this work, we numerically simulate the accretion of objects in the MAB region during the time when gas in the protoplanetary disk still existed while assuming different MAB primordial masses. We then account for the depletion of that population happening after gas disk dispersal. In our analysis, we subdivided the MAB into five subregions and showed that the depletion factor varies throughout the MAB. This results in uneven radial- and size-dependent depletion of the MAB. We show that the MAB primordial mass has to be  $\lesssim 2.14 \times 10^{-3} M_{\oplus}$ . Larger primordial masses would lead to the accretion of tens to thousands of S-complex objects with  $D > 500$  km in the MAB. Such large objects would survive depletion even in the outer subregions ( $a > 2.5$  au), thus being inconsistent with observations. Our results also indicate that S-complex objects with  $D > 200$ –300 km, including (4) Vesta, are likely to be terrestrial planetesimals implanted into the MAB rather than formed in situ.

*Unified Astronomy Thesaurus concepts:* [Asteroid belt \(70\)](#); [Asteroid dynamics \(2210\)](#); [Solar system formation \(1530\)](#)

## 1. Introduction

The main asteroid belt (MAB), situated between the orbits of Mars and Jupiter, contains over 1 million objects with diameter  $D$  larger than  $\approx 1$  km (Bottke et al. 2020). It also has a cumulative mass of only about 1/2000 that of Earth ( $\approx 5 \times 10^{-4} M_{\oplus}$ ; DeMeo & Carry 2013, 2014, where  $M_{\oplus}$  represents 1 Earth mass). The reason why the MAB has such a tiny total mass has been, for years, a subject of debate in the literature (e.g., Wetherill 1980; Chambers 2001; Raymond et al. 2006; Walsh et al. 2011; Izidoro et al. 2015; Roig & Nesvorný 2015; Deienno et al. 2016, 2018, 2022; Nesvorný et al. 2017; Clement et al. 2019).

The MAB can be characterized using two broad taxonomic groupings of asteroids, S- and C-complex (Gradie & Tedesco 1982; Mothé-Diniz et al. 2003; DeMeo & Carry 2014). Spectroscopic analysis (Burbine et al. 2002) shows the S-complex to be relatively dry, with less than 0.1% water by mass, and many constituents are related to inner solar system ordinary chondrites (Robert et al. 1977; Che & Zega 2023). Many C-complex bodies, on the other hand, potentially carry about 5%–20% water by mass content and seem more akin to outer solar system carbonaceous chondrites (Kerridge 1985; Che & Zega 2023). The radial distance from the star where the division between the inner and outer solar system occurred early in solar system history is poorly defined. The mechanism responsible for dividing the two primordial solar system

reservoirs that sourced these distinct taxonomic classes is also a matter of debate (e.g., Kruijjer et al. 2017, 2020; Brasser & Mojzsis 2020; Johansen et al. 2021; Lichtenberg et al. 2021; Izidoro et al. 2022; Morbidelli et al. 2022). However, there is a consensus in the literature that water/volatile-poor (S-complex) and water/volatile-rich (C-complex) groups formed in the regions interior and exterior to the orbit of Jupiter, respectively (e.g., Hellmann et al. 2023).

Several works in the literature (e.g., Walsh et al. 2011, 2012; Roig & Nesvorný 2015; Deienno et al. 2016, 2018; Izidoro et al. 2016; Raymond & Izidoro 2017a, 2017b; Nesvorný et al. 2017; Clement et al. 2019; Lykawka & Ito 2023, to cite a few) have attempted to find dynamical models that can reproduce both the low mass and taxonomic mixing observed in the current MAB. In general, these models largely agree with the above interpretation that the MAB's taxonomic distribution can be reproduced if the S- and C-complex groups are assumed to have formed in regions interior and exterior to the orbit of Jupiter, respectively, and were transported into the MAB at later stages after their formation. The same models, however, disagree about the amount of primordial mass in solids that populated the MAB prior to the implantation of planetesimals (Raymond & Izidoro 2017a, 2017b).

There are currently two different views for explaining the MAB's low mass. On one side, it was proposed that solids in the protoplanetary disk followed a smooth radial distribution of mass (Weidenschilling 1977; Hayashi 1981), and as a result, the primordial MAB was composed of several Earth masses. In this case, the MAB's primordial mass had to have been severely depleted at the earliest stages of the solar system history. Early depletion seems necessary to reproduce the



Original content from this work may be used under the terms of the [Creative Commons Attribution 4.0 licence](#). Any further distribution of this work must maintain attribution to the author(s) and the title of the work, journal citation and DOI.

abundance of highly siderophile elements measured on the crust and mantle of asteroid (4) Vesta (Zhu et al. 2021).

Early depletion of the MAB (while gas in the protoplanetary disk still existed) could happen in the following ways. Disk–planet tidal interactions (e.g., Nelson 2018) could potentially lead to a putative early migration episode for Jupiter and Saturn (Walsh et al. 2011). Alternatively, convergent migration of growing protoplanets could result in large objects forming exterior to 1.5 au to migrate toward 1 au (Brož et al. 2021; Woo et al. 2023). In both cases, most of the preexisting objects between 1.5 and 4 au would be removed during the gas disk’s lifetime, thus leading to an early depletion of the MAB region. How early is early in these models depends on many disk parameters, with the real answer poorly constrained.

After gas disk dispersal, early MAB depletion (i.e., during terrestrial planet formation; Clement et al. 2018; see also Nesvorný et al. 2021) may occur in the following ways. A violent giant planet dynamical instability (Clement et al. 2019)<sup>4</sup> would lead to about 99.9% depletion of the MAB primordial mass. Alternatively, Jupiter and Saturn, while locked in 2:1 mean-motion resonance (MMR) with eccentric orbits (Clement et al. 2021a, 2021b), would induce chaotic evolution of secular resonances within the MAB region (Izidoro et al. 2016). Both models could lead to the depletion of the MAB on timescales of the order of 5–10 Myr after gas disk dispersal (Clement et al. 2018; Lykawka & Ito 2023).

The story is much simpler if the primordial MAB was partially or fully devoid of material initially (e.g., Hansen 2009; Izidoro et al. 2015). This scenario is supported by cosmochemical evidence (e.g., Warren 2011; Bollard et al. 2017; Kruijer et al. 2017, 2020; Nanne et al. 2019; Spitzer et al. 2020; Burkhardt et al. 2021) suggesting that the solar system’s building blocks formed in concentric rings at various radial distances around the Sun (Izidoro et al. 2022; Morbidelli et al. 2022), similar to ring-structured protoplanetary disks observed by the Atacama Large Millimeter/submillimeter Array (e.g., Andrews et al. 2018; Huang et al. 2018). In this case, the observed total mass of the MAB would result from the implantation of asteroids of S- and C-complex taxonomic classes (Raymond & Izidoro 2017a, 2017b; see also Nesvorný et al. 2024) combined with the mass of S-complex primordial asteroids that formed in the MAB region. The total implanted mass (combined with the MAB primordial mass), however, likely never exceeded 10 times the current MAB’s total mass, as giant planet dynamical instabilities that were well tested against outer solar system constraints often provide only about 75%–90% overall depletion rates (Roig & Nesvorný 2015; Deianno et al. 2016, 2018, 2022; Nesvorný et al. 2017). Alternatively, models of pebble accretion (Levison et al. 2015a; Johansen et al. 2015) could also lead to the formation of a low-mass MAB. In this scenario, the distinction between where S- and C-complex asteroids would form and their mixing into the MAB region, however, is less clear, as all asteroids (planetesimals) would potentially form out of the same pebble flux.

It is clear from the discussion presented in the previous paragraphs that the primordial amount of mass that initially existed in the MAB is a key ingredient to dictate the formation and early evolution of the solar system. Ideally, we would like

<sup>4</sup> Often associated with evolutionary paths where Jupiter and Saturn acquire highly eccentric orbits and do not necessarily satisfy outer solar system constraints (Nesvorný & Morbidelli 2012; Deianno et al. 2017).

to account for both collisional and dynamical evolution (and depletion) in a self-consistent way using modern ideas about how the MAB was affected by early solar system processes. The majority of the work discussed so far assumed that (i) mass depletion was driven by dynamical effects, (ii) asteroids were assumed to be massless test particles, and (iii) collisional evolution was not included (i.e., growth and fragmentation). The few works that accounted for collisional evolution of the MAB (e.g., Bottke et al. 2005a; Morbidelli et al. 2009) mostly concentrated on understanding the evolution of the MAB size–frequency distribution (SFD) but with limited dynamical effects (i.e., assuming that MAB collision probabilities and impact velocities were nearly constant through the age of the solar system) or with models that do not reflect present-day thinking on the problem (i.e., assuming that protoplanets formed in the asteroid belt; Bottke et al. 2005b). Given that many of these works did not directly account for dynamical depletion, the amount of primordial mass that may have existed in the MAB is difficult to constrain. Therefore, to advance in our understanding of not just where but how planetesimals formed and how planets evolved in the early history of the solar system, it is crucial that we understand how much mass existed in the MAB region after planetesimals formed. To do that, it is important that we consider not only the MAB’s total mass but also its SFD.

Only three objects in the current MAB have  $D > 500$  km. These are the asteroids (1) Ceres, (2) Pallas, and (4) Vesta (e.g., Bottke et al. 2005a, 2020). The first two (a B-type and a C-type, respectively; DeMeo et al. 2009) are in the C-complex and probably originated from orbits beyond Jupiter (e.g., Hellmann et al. 2023). In fact, the formation location of asteroid (2) Pallas is poorly understood, but (1) Ceres has recently been proposed to originate beyond Saturn’s orbit (Ribeiro de Sousa et al. 2022). This would help explain the ammonia signatures found on its surface (de Sanctis et al. 2015). Asteroid (4) Vesta (a V-type; DeMeo et al. 2009) is the sole  $D > 500$  km object that is a member of the S-complex.<sup>5</sup> It is therefore associated with objects originating from orbits interior to that of Jupiter. Its existence provides a useful constraint on the number of  $D > 500$  km bodies that could have formed, or grown, within the primordial MAB. In other words, the primordial mass of the MAB cannot be such that accretion would lead to the formation of too many S-complex objects with  $D > 500$  km. If this had been the case, it is possible that more than one could survive solar system evolution and would be observed at the present day. This is clearly not the case.

In this work, we followed the accretion of planetesimals in the MAB region as a function of their initial total mass and accretion time. We also considered cases with and without Jupiter in the simulations. Our primordial MAB SFD is based on the findings of Morbidelli et al. (2009; see Section 2 for discussion). We compare our results with the current number of objects with  $D > 500$  km that would (i) form during the lifetime of the gaseous solar nebula (3 or 5 Myr, based on the relative ages of ordinary and CB chondrites, respectively; Krot et al. 2005; Pape et al. 2019; see also Weiss et al. 2021 regarding paleomagnetism constraints) and (ii) survive the

<sup>5</sup> Note that in this work, we loosely define S-complex asteroids as any noncarbonaceous objects, including (4) Vesta. We will return to this issue and thoroughly discuss the reasons behind our generically defined taxonomic classification and related implications in Section 4.2, where they will become more relevant.

aftermath of the giant planet instability (Nesvorný & Morbidelli 2012; Deienno et al. 2017, 2018; Nesvorný et al. 2017; Clement et al. 2019), as well as (iii) chaotic diffusion during subsequent solar system evolution (Minton & Malhotra 2010; see also Deienno et al. 2016, 2018, 2022). We show that, unless the primordial mass of the MAB was indeed very low ( $\lesssim 2.14 \times 10^{-3} M_{\oplus}$ )<sup>6</sup> before accretion started, the number of S-complex objects with  $D > 500$  km that would form and survive solar system evolution largely exceeds the number currently observed (i.e.,  $N_{\text{S-complex}}(D > 500 \text{ km}) = 1$ ; (4) Vesta; Bottke et al. 2005a, 2020).

We present our work in the following structure. Section 2 describes our modeling. In Section 3, we describe how we have chosen the data set for comparison between model results and the currently observed MAB. Our results are presented in Section 4, and conclusions are in Section 5.

## 2. Model

To model the evolution of the MAB SFD and the accretion of planetesimals with  $D > 500$  km in the MAB region, we first assume that planetesimals were formed within the first 0.5 Myr after calcium-aluminum-rich inclusions (CAIs) based on the methods by Izidoro et al. (2022; see also Lichtenberg et al. 2021; Morbidelli et al. 2022). Therefore, our simulations started at  $t = 500$  kyr. As for the initial SFD of our planetesimal population, we followed Morbidelli et al. (2009; see also Bottke et al. 2005a). Although we have some knowledge of the cumulative slope of the SFD for Kuiper Belt objects (e.g., Fraser et al. 2014), not much is known about the SFD of planetesimals that formed in the MAB region (e.g., Simon et al. 2016). However, we know from Bottke et al. (2005a) and Morbidelli et al. (2009) that the current MAB SFD for objects with  $D > 100$  km can only be reproduced if the MAB SFD cumulative slope right after gas disk dispersal was the same as that observed in the current MAB for objects with sizes in the range  $100 \text{ km} < D < 500 \text{ km}$  (Figure 1). We acknowledge that the primordial MAB SFD may not necessarily be the same as that from the end of the gas disk phase (e.g., Johansen et al. 2015; Simon et al. 2016). Similarly, we acknowledge that different combinations of initial SFD and disruption laws could lead to the conditions reported in Morbidelli et al. (2009; see Bottke et al. 2020). Yet, for simplicity, and to avoid an extensive amount of work dedicated specifically to the combination of initial SFD and disruption laws that would lead to the finds by Morbidelli et al. (2009), we decided to assume that the current cumulative slope of the MAB SFD in the range  $100 \text{ km} < D < 500 \text{ km}$  is primordial. We also considered, for consistency, the collision evolution parameters related to basalt targets from Benz & Asphaug (1999; i.e., the same disruption law considered by Morbidelli et al. 2009). Our results should then be taken with these caveats in mind. We also do not consider pebble accretion in our modeling due to the distinction in the forming regions of S- and C-complex planetesimals that we adopted. Nonetheless, in term of primordial MAB mass, pebble accretion models should likely lead to similar conclusions.

For the total primordial mass of the MAB, we assumed that the initial distribution of planetesimals, uniformly distributed

<sup>6</sup> Or eventually depleted to this level before accretion starts, i.e., during the first few hundred kyr after planetesimals formed, while still in the gas disk phase.

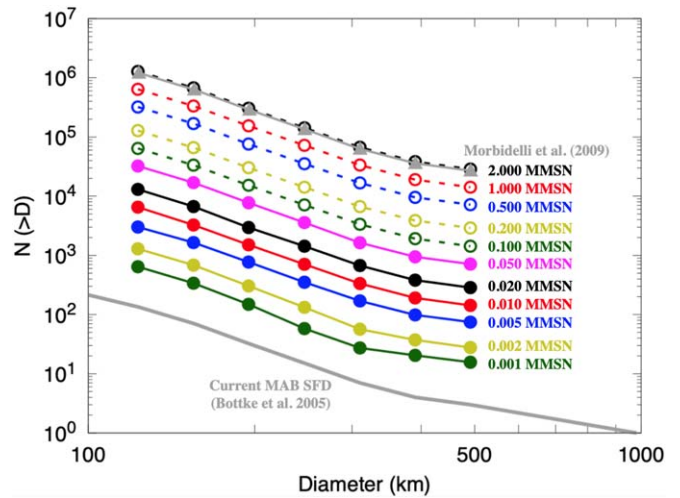


**Figure 1.** Initial cumulative SFDs adopted for our different primordial MAB populations in terms of MMSN (see main text). For reference, we show (1) a gray line at the bottom representing the current MAB SFD from Bottke et al. (2005a) and (2) gray triangles from Figure 7(a) in Morbidelli et al. (2009). Other colored symbols/lines are for the different primordial MAB masses considered in term of MMSN. From top to bottom: 2.000 MMSN (black), 1.000 MMSN (red), 0.500 MMSN (blue), 0.200 MMSN (yellow), 0.100 MMSN (green), 0.050 MMSN (magenta), 0.020 MMSN (black), 0.010 MMSN (red), 0.005 MMSN (blue), 0.002 MMSN (yellow), and 0.001 MMSN (green). See the main text for the actual mass in Earth masses for each specific case.

between 1.8 and 3.6 au (Deienno et al. 2016, 2018), follows a density profile  $\Sigma = \Sigma_0 r^{-\gamma}$ , which is analogous to the minimum-mass solar nebula (MMSN; Hayashi 1981) radial density profile, and for simplicity, we refer to it as such. We chose  $\gamma = 1$  (following values derived from observations of protoplanetary disks; e.g., Andrews et al. 2010) and a stellar metallicity of 1% to determine the total mass in solids. We also assumed that only a fraction of the total solid mass was converted into planetesimals ( $f_{\text{pl}} = 0.2$ ; e.g., Levison et al. 2015a, 2015b; Johansen et al. 2019; Deienno et al. 2022).  $\Sigma_0$  in  $\Sigma = \Sigma_0 r^{-1}$  is defined as  $\zeta \Sigma_{1\text{au}}$ , where  $\Sigma_{1\text{au}}$  represents the MMSN surface density at 1 au, equal to  $1700 \text{ g cm}^{-2}$  (Hayashi 1981). We considered five different values for  $\Sigma_0$  with  $\zeta = 0.001, 0.002, 0.005, 0.01, 0.02, 0.05, 0.1, 0.2, 0.5, 1$ , and  $2$ .<sup>7</sup> This range of parameters results in simulations of MAB primordial masses with initial  $M_{\text{disk}} \approx 0.001, 0.003, 0.007, 0.013, 0.027, 0.068, 0.13, 0.27, 0.68, 1.35$ , and  $2.71 M_{\oplus}$ .<sup>8</sup> Planetesimals were initially placed in nearly circular and planar orbits with randomized orbital angles (Deienno et al. 2018; Clement et al. 2019). Figure 1 shows the initial cumulative SFDs adopted for our different primordial MAB populations in terms of MMSN.

<sup>7</sup> Considering more values of  $f_{\text{pl}}$  or  $\Sigma_0$  is not necessary because the values of the total disk mass would overlap; e.g.,  $M_{\text{disk}}$  is the same when comparing the pairs (0.1 MMSN;  $f_{\text{pl}} = 0.2$ ) with (0.2 MMSN;  $f_{\text{pl}} = 0.1$ ), or (0.5 MMSN;  $f_{\text{pl}} = 0.1$ ) with (0.1 MMSN;  $f_{\text{pl}} = 0.5$ ), and so on. Therefore, performing simulations with intermediate cases (more values of  $f_{\text{pl}}$  and  $\Sigma_0$ ) would not necessarily improve or change the results and conclusions.

<sup>8</sup> Note that (1) these latter values ( $\geq 1$  MMSN) are similar to the surface density at  $\approx 1$  au presumably required to form Earth and Venus (e.g., Chambers 2001; Clement et al. 2018; Walsh & Levison 2019), whereas (2) the former values ( $< 1$  MMSN) are consistent with disk models that find that planetesimal formation is inefficient in the MAB (e.g., Drazkowska & Dullemond 2018; Lichtenberg et al. 2021; Izidoro et al. 2022; Morbidelli et al. 2022).

The exact time and radial distance of Jupiter’s formation is unknown (e.g., Chambers 2021; Deianno et al. 2022). We considered cases with and without the gravitational influence of Jupiter in our simulations while following planetesimal accretion during the gas disk phase. The reason for this choice is to test two end-member cases. When considering the effects of Jupiter’s gravitational perturbations, we opted to keep Jupiter’s semimajor axis fixed near 5.4 au (Jupiter’s pre-giant-planet instability position is often assumed to be anywhere between 5.4 and 6 au; e.g., Nesvorný & Morbidelli 2012; Deianno et al. 2017; Clement et al. 2018; Lykawka & Ito 2023). Not having Jupiter is the same as having it very far away for a long time, whereas having it fixed at 5.4 au is similar to having it form early and/or rapidly migrate to its preinstability orbit (e.g., Chambers 2021; although still within reasonable distances, Deianno et al. 2022, i.e., with  $a \lesssim 10\text{--}15$  au). Lastly, for the simulations where we accounted for Jupiter’s perturbations, it is important to acknowledge that, as we cannot self-consistently model the hydrodynamical effects of the gas disk acting on Jupiter, for simplicity, we assumed an initially circular and planar orbit. Additionally, as Saturn is not included in the simulations, we cannot account for any induced effects in the MAB region, like chaos arising from the interaction of eccentric Jupiter and Saturn, while these worlds reside in their mutual 2:1 MMR (Izidoro et al. 2016; Lykawka & Ito 2023). Still, this approximation may be reasonable, with chaotic effects only expected to become important 5–10 Myr after gas disk dispersal (Izidoro et al. 2016). We also do not know how long it takes for Jupiter and Saturn to be captured in mutual MMRs and thereby develop significant eccentricities (e.g., Pierens & Raymond 2011; Pierens et al. 2014). Adding additional complexity to this problem would not necessarily improve our results, but that is an issue that can be more thoroughly tested in future works.

We followed the accretion of objects within our MAB region for 5 Myr. This interval is presumably the time the gas in the solar nebula dispersed in the outer solar system based on the relative ages of the youngest CB chondrites to CAIs (Krot et al. 2005). As chondrules may only form and get incorporated into planetesimals while gas still exists in the solar nebula (Johnson et al. 2016), the date of the youngest (latest formed) chondrules are possibly representative of when gas in the protoplanetary nebula may have dispersed for the zone where those chondrules formed. Those ages are also in good agreement with paleomagnetism constraints, suggesting that the nebular gas dispersal time in the inner and outer solar system was approximately  $1.22 \text{ Myr} < T_{\text{inner}}^{\text{gas}} < 3.94 \text{ Myr}$  and  $2.51 \text{ Myr} < T_{\text{outer}}^{\text{gas}} < 4.89 \text{ Myr}$  (Weiss et al. 2021). We also consider that the gas in the solar nebula dispersed following an exponential timescale (i.e., gas decays as  $\exp(-t/\tau_{\text{gas}})$ ; Haisch et al. 2001). We assumed  $\tau_{\text{gas}} = 2 \text{ Myr}$  (the average timescale commonly assumed in planet formation and early solar system evolution theories; e.g., Bitsch et al. 2015a, 2015b; Levison et al. 2015a, 2015b; Walsh & Levison 2016, 2019; Johansen & Lambrechts 2017; Deianno et al. 2019, 2022; Johansen et al. 2019, 2021; Brož et al. 2021; Izidoro et al. 2021, 2022). Additional tests for  $\tau_{\text{gas}} = 0.5$  and 1 Myr produced no substantial differences in our results. For this reason, in Section 4, we only report on simulations with  $\tau_{\text{gas}} = 2 \text{ Myr}$ .

To follow the dynamics and accretion of the MAB under the considerations above, we used the code known as Lagrangian

Integrator for Planetary Accretion and Dynamics (LIPAD; Levison et al. 2012). As previously described (e.g., Deianno et al. 2022, and references therein), LIPAD is a particle-based (i.e., Lagrangian) code that can follow the collisional/accretion/dynamical evolution of a large number of sub-kilometer objects throughout the entire growth process to become planets. It uses the concept of tracer particles to represent a large number of small bodies with roughly the same orbit and size (see Levison et al. 2012 for more specific details of the code). LIPAD has a prescription for the gaseous nebula from Hayashi et al. (1985). This gas disk provides aerodynamic drag, eccentricity, and inclination damping on planetesimals and planets. The collisional routines from LIPAD use the Benz & Asphaug (1999) disruption laws (see discussion at the beginning of this section). LIPAD is a well-tested code that has been successfully employed in previous studies following the collisional evolution and accretion of centimeter- to kilometer-sized planetesimals on their way to becoming planets (Kretke & Levison 2014; Levison et al. 2015a, 2015b; Walsh & Levison 2016, 2019; Deianno et al. 2019, 2020, 2022; Voelkel et al. 2021a, 2021b; Izidoro et al. 2022), making it ideal for our investigation of the evolution of the MAB SFD while accounting for dynamical effects.

All planetesimals within all tracer particles are allowed to have self-gravitational interactions and to collide with one another throughout the simulation. We discarded objects that collisionally evolved to sizes below 1 mm, assuming those would rapidly grind down to dust and no longer contribute to the accretion process (Deianno et al. 2020, 2022).

### 3. MAB, Data Set, and Comparison with the Minor Planet Center

After we follow accretion in the MAB during the first 5 Myr of the solar system’s history, it is necessary to account for the various processes that happened during the subsequent 4.5 Gyr of evolution after gas disk dispersal. Specifically, the giant planet instability has been found to heavily deplete the MAB (Roig & Nesvorný 2015; Deianno et al. 2016, 2018; Clement et al. 2019). Chaotic diffusion leads to an additional 50% of depletion (Minton & Malhotra 2010). Below, we gather and reduce numerous works that have simulated the depletion effects of the giant planet instability and map that depletion to different regions in the MAB. This provides an important tool for comparison between formation simulations from this work with observations of the current-day MAB.

In this work, we consider the MAB region to be delimited as follows (e.g., Deianno et al. 2018; see also Roig & Nesvorný 2015; Nesvorný et al. 2017; Clement et al. 2019 for similar but slightly different MAB definitions):  $i < 20^\circ$ ,  $q > 1.9 \text{ au}$ ,  $a < 3.6 \text{ au}$ , and  $Q < 4.1 \text{ au}$ . We want to avoid objects with  $q < 1.9 \text{ au}$  and  $Q > 4.1 \text{ au}$ ; objects on these orbits are likely to have close encounters with Mars and Jupiter, respectively, and their orbits may wander in the  $a - e$  and  $a - i$  planes. We also do not want any overlap with the Hilda population (semimajor axis centered at  $\approx 4.1 \text{ au}$ ; e.g., Roig & Nesvorný 2015). We capped the inclination distribution at  $i < 20^\circ$ , as numerical simulations of the orbital evolution of the MAB during the giant planet instability often tend to overpopulate regions with  $i > 20^\circ$  (Deianno et al. 2016, 2018; Nesvorný et al. 2017; Clement et al. 2019, 2020). These orbital parameter cutoffs allow us to directly compare results with what we may define as the core of the MAB.

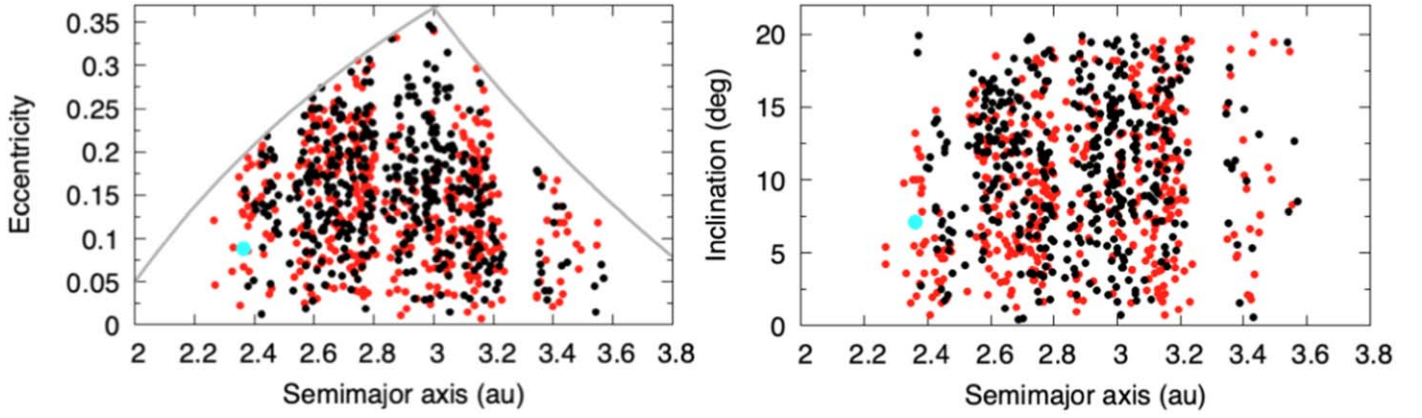


**Figure 2.** Comparison between the current MAB (see main text for our definition of the MAB) from MPC with  $H < 9.6$  (red) and results from Deianno et al. (2018; black). Left: eccentricity vs. semimajor axis. Gray lines demarcate regions where  $q = 1.9$  au and  $Q = 4.1$  au. Right: inclination vs. semimajor axis. The cyan dot represents the real orbit of asteroid (4) Vesta taken from the MPC data.

**Table 1**  
Columns Represent Subregions of the MAB (see Main Text)

MPC $N_{\text{ast}}$	EiMB	IMB	CMB	OMB	EoMB	MAB
D18 $N_{\text{ast}}^{\text{final}}$	0	28	162	221	19	430
D18 $N_{\text{ast}}^{\text{initial}}$	1111	2222	1777	2389	1944	9443
D18 $D_{\text{fac}} (\times 10^{-2})$	0.000	1.260	9.116	9.251	0.977	4.553
D18 $D_{\text{per}} (\%)$	100.000	98.740	90.884	90.749	99.023	95.447
C19 <sub>all</sub> $N_{\text{ast}}^{\text{final}}$	6	67	90	263	51	477
C19 <sub>all</sub> $N_{\text{ast}}^{\text{initial}}$	1872	7241	6526	7696	7306	30641
C19 <sub>all</sub> $D_{\text{fac}} (\times 10^{-2})$	0.320	0.925	1.379	3.417	0.698	1.557
C19 <sub>all</sub> $D_{\text{per}} (\%)$	99.680	99.075	98.621	96.583	99.302	98.443
C19 <sub><math>P_S/P_I</math></sub> $N_{\text{ast}}^{\text{final}}$	0	4	28	188	45	265
C19 <sub><math>P_S/P_I</math></sub> $N_{\text{ast}}^{\text{initial}}$	432	1671	1506	1776	1686	7071
C19 <sub><math>P_S/P_I</math></sub> $D_{\text{fac}} (\times 10^{-2})$	0.000	0.239	1.859	10.586	2.669	3.748
C19 <sub><math>P_S/P_I</math></sub> $D_{\text{per}} (\%)$	100.000	99.761	98.141	89.414	97.331	96.252

**Note.** MPC  $N_{\text{ast}}$  refers to the current number of asteroids in each MAB subregion from the MPC data. Simulation data from different works in the literature is provided in sets of four rows. D18 refers to the work by Deianno et al. (2018; our fiducial case and similar to the findings from Roig & Nesvorný 2015; Deianno et al. 2016; Nesvorný et al. 2017), while C19 refers to the work by Clement et al. (2019; for a potential upper limit in depletion). Labels  $N_{\text{ast}}^{\text{initial}}$  and  $N_{\text{ast}}^{\text{final}}$  are for the number of asteroids initially placed in each MAB subregion and those who survived depletion, respectively, in each work.  $D_{\text{fac}}$  represents the depletion factor reported once accounting for the ratio  $D_{\text{fac}} \approx N_{\text{ast}}^{\text{final}}/N_{\text{ast}}^{\text{initial}}$ .  $D_{\text{fac}}$  effectively reports the survival fraction of objects from the simulation. Yet we prefer to refer to them as a depletion factor, as those are the numbers by which we directly multiply the evolved population in order to account for their depletion.  $D_{\text{per}} \approx 100 \times (1 - D_{\text{fac}})$ . Labels all and  $P_S/P_I$  are for different cuts in the data by Clement et al. (2019; see main text).

We then use this MAB definition to select objects from the Minor Planet Center (MPC) database<sup>9</sup> having  $H < 9.6$ , which should correspond to objects with  $D \gtrsim 50$  km (assuming an averaged geometric albedo  $\langle p_v \rangle = 0.1$ ). We use objects with  $D \gtrsim 50$  km to avoid contamination from main-belt fragments likely formed from catastrophic collisions (Michel et al. 2001; Durda et al. 2007; Nesvorný et al. 2015, 2017). Figure 2 shows the comparison between real objects taken from MPC and results taken from Deianno et al. (2018) within the previously defined limits of the MAB. Data from Deianno et al. (2018; see also Roig & Nesvorný 2015; Nesvorný et al. 2017; Clement et al. 2019, 2020 for additional comparison) were obtained while modeling the excitation and depletion of the MAB

through the giant planet instability (Nesvorný & Morbidelli 2012; Deianno et al. 2017) followed by a subsequent 4.5 Gyr of solar system evolution to account for loss due to chaotic diffusion of long-term unstable orbits (Minton & Malhotra 2010).

Figure 2 shows very good agreement between the results from Deianno et al. (2018) and real data from MPC (compare also the numbers from rows labeled MPC  $N_{\text{ast}}$  and D18  $N_{\text{ast}}^{\text{final}}$  from Table 1) while accounting for the necessary effects happening during the 4.5 Gyr after gas disk dispersal as listed in the beginning of this section. For those reasons, and because the results presented in Figure 2 are derived from simulations that self-consistently satisfied several outer solar system constraints (Nesvorný & Morbidelli 2012; Deianno et al. 2014, 2017; Nesvorný 2015a, 2015b), we refer to data from Deianno et al. (2018) as our fiducial case when

<sup>9</sup> Data obtained on 2023 March 2, at <https://minorplanetcenter.net/iau/MPCORB.html>.

estimating the depletion of the MAB due to the giant planet instability followed by 4.5 Gyr of subsequent evolution.

For our depletion analysis, we further divide the MAB definition above into five subregions: extended inner main belt (EiMB;  $a < 2.1$  au), inner main belt (IMB;  $2.1 \text{ au} < a < 2.5$  au), center main belt (CMB;  $2.5 \text{ au} < a < 2.82$  au), outer main belt (OMB;  $2.82 \text{ au} < a < 3.25$  au), and extended outer main belt (EoMB;  $a > 3.25$  au). The row labeled D18  $D_{\text{fac}}$  in Table 1 shows what the depletion factor is in each of these MAB subregions from Deienno et al. (2018). Table 1 also reports on the number of asteroids per MAB subregion in data from both MPC (MPC  $N_{\text{ast}}$ ) and the surviving asteroids from simulations by Deienno et al. (2018; D18  $N_{\text{ast}}^{\text{final}}$ ; values plotted in Figure 2). D18  $N_{\text{ast}}^{\text{initial}}$  represents the number of initial asteroids in the data from Deienno et al. (2018) used for calculating the corresponding depletion factors. The percentage of depletion (D18  $D_{\text{per}}$ ) in each subregion as well as in the entire MAB is also presented for reference.

As previously discussed, the MAB is heavily depleted by the giant planet instability. The level of depletion depends strongly on the number of planet–planet close encounters and the specific orbital evolution of the giant planets, mostly Jupiter, during the giant planet instability. In regard to the MAB evolution and depletion, the most important constraints to satisfy are Jupiter’s orbital eccentricity and Jupiter and Saturn’s period ratio ( $P_S/P_J$ ). Only some giant planet instability simulations, however, are able to satisfy such constraints (see Nesvorný 2018 for a comprehensive review of giant planet instability constraints). Yet the MAB depletion factor is also highly dependent on the definition of the MAB region. The works by Roig & Nesvorný (2015), Deienno et al. (2016, 2018), and Nesvorný et al. (2017), for example, while relying on a small number of simulations that satisfy the constraints, report an overall mass depletion of about 75%–90% for an MAB delimited only by  $q > 1.9$  au and  $a < 3.2$  au. Once further truncating and narrowing the MAB to its core, as shown in Figure 2 for direct comparison with the MPC catalog, those same giant planet instability simulations lead to an overall depletion of approximately 95.45% (Table 1, D18  $D_{\text{per}}$  MAB). Alternatively, the work by Clement et al. (2019) adopted a broader limit for the MAB region in the range  $2 \text{ au} \leq a \leq 4 \text{ au}$ . That work also relied strongly on the accumulated statistical effects from multiple giant planet instability evolutions without focusing on specific constraints (as done in Roig & Nesvorný 2015; Deienno et al. 2016, 2018; Nesvorný et al. 2017). The resulting overall MAB depletion was reported to be 99.9%. Although the methodology applied by Clement et al. (2019) is valid, it remains to be confirmed that giant planet instabilities leading up to 99.9% depletion of the MAB are consistent, not only with constraints related to Jupiter’s eccentricity and  $P_S/P_J$  but also with other solar system constraints obtained from observations of Jupiter Trojans, the giant planets’ regular and irregular satellites, and Kuiper Belt objects (Nesvorný & Morbidelli 2012; Deienno et al. 2014, 2017; Nesvorný 2015a, 2015b; which are satisfied in the instability simulation by Deienno et al. 2018). Yet, for completeness, in this work (see also Deienno et al. 2022), we will consider results from Clement et al. (2019) using the following two restrictive definitions (for cases presented in Table 1).

1. C19<sub>all</sub> refers to results taken from Clement et al. (2019) while excluding runs 4, 7, and 7a,<sup>10</sup> as well as those with embryos (runs 1b and 2b).<sup>11</sup>
2. C19 <sub>$P_S/P_J$</sub> <sup>AMD<sub>JS</sub></sup> is also for results from Clement et al. (2019) but while only considering cases where  $\text{AMD}_{\text{JS}} < 0.1$ <sup>12</sup> and  $2.3 \lesssim P_S/P_J \lesssim 2.5$ <sup>13</sup> at the end of the giant planet instability phase (runs 1, 2a, and 5a).

The work by Clement et al. (2019) reported on MAB depletion within a few hundred Myr after the end of the giant planet instability, and they did not account for the 50% additional depletion during the subsequent 4.5 Gyr of solar system evolution. For consistency, we divided the asteroid number count by 2 when calculating values for C19<sub>all</sub> and C19 <sub>$P_S/P_J$</sub> <sup>AMD<sub>JS</sub></sup> in each MAB subregion. These are the final numbers presented in Table 1. We refer to the Clement et al. (2019) depletion factor as C19<sub>all</sub>  $D_{\text{fac}}$  and C19 <sub>$P_S/P_J$</sub> <sup>AMD<sub>JS</sub></sup>  $D_{\text{fac}}$ . The new percentage of depletion from Clement et al. (2019) after these cuts is in much closer agreement with the data by Deienno et al. (2018, and references therein), with C19<sub>all</sub>  $D_{\text{per}} \approx 98.44\%$  and C19 <sub>$P_S/P_J$</sub> <sup>AMD<sub>JS</sub></sup>  $D_{\text{per}} \approx 96.25\%$  (not 99.9%, as previously reported at the end of the giant planet instability<sup>14</sup>). C19 cases also present a larger asteroid number difference per MAB subregion once comparing C19<sub>all</sub>  $N_{\text{ast}}^{\text{final}}$  and C19 <sub>$P_S/P_J$</sub> <sup>AMD<sub>JS</sub></sup>  $N_{\text{ast}}^{\text{final}}$  with MPC  $N_{\text{ast}}$  than D18  $N_{\text{ast}}^{\text{final}}$ . For this reason, and given the larger values for C19<sub>all</sub>  $D_{\text{per}}$  and C19 <sub>$P_S/P_J$</sub> <sup>AMD<sub>JS</sub></sup>  $D_{\text{per}}$  compared to D18  $D_{\text{per}}$ , we consider the C19<sub>all</sub>  $D_{\text{fac}}$  and C19 <sub>$P_S/P_J$</sub> <sup>AMD<sub>JS</sub></sup>  $D_{\text{fac}}$  values to be an upper limit for depletion one could expect once accounting for the effects of the giant planet instability and subsequent solar system evolution.

Our analyses clearly demonstrate that MAB depletion during the giant planet instability is not uniform. The fact that different MAB subregions have different depletion factors was first pointed out by Nesvorný et al. (2017) but never quantified in detail. Table 1 shows that, regardless of the data used, both Deienno et al. (2018) and Clement et al. (2019) report much larger depletion for the EiMB and EoMB than for any other subregion. In fact, the EiMB is likely to always be fully depleted (e.g., Bottke et al. 2012; Nesvorný et al. 2017). A very large depletion is also expected in the IMB, as the powerful  $\nu_6$  secular resonance (resulting from commensurable rates between Saturn’s and asteroids’ precession frequencies) must cross the IMB region in any formation scenario (Morbidelli et al. 2010). It is also noticeable that the CMB and OMB

<sup>10</sup> Cases 4, 7, and 7a (see Figure 2 and Table 2 presented in the work by Clement et al. 2019) can be ruled out, as they result in final orbital excitation and separation of Jupiter and Saturn that are orders of magnitude above the observed values, which in turn lead to 100% depletion of the entire MAB.

<sup>11</sup> As noted by Clement et al. (2019; see also O’Brien et al. 2007), their simulations struggled in depleting all planetary embryos inserted into the MAB, thus potentially adding unrealistic perturbations that would likely lead to an overestimation of  $D_{\text{per}}$ .

<sup>12</sup> The current AMD (Laskar 1997) of Jupiter and Saturn ( $\text{AMD}_{\text{JS}}$ ) is about 0.0015. Here we consider  $\text{AMD}_{\text{JS}} < 0.1$  a good proxy because this value is expected to lower during a 100–200 Myr period after the giant planet instability due to dynamical friction exerted by planetesimals interacting with those planets (Nesvorný & Morbidelli 2012; Deienno et al. 2017).

<sup>13</sup>  $P_S/P_J \approx 2.49$  in the current solar system configuration (Nesvorný & Morbidelli 2012). In this cut, we also avoided the range  $2.1 \lesssim P_S/P_J \lesssim 2.3$  because in such a case, Jupiter and Saturn’s secular and MMRs would be largely misplaced, thus leading to unseen signatures in the MAB orbital structures (Morbidelli et al. 2010; Deienno et al. 2016, 2018).

<sup>14</sup> Not accounting for the additional 50% depletion factor, as presented by Clement et al. (2019), would lead to C19<sub>all</sub>  $D_{\text{per}} \approx 96.87\%$  and C19 <sub>$P_S/P_J$</sub> <sup>AMD<sub>JS</sub></sup>  $D_{\text{per}} \approx 92.50\%$ , whose values are then in even closer agreement with Roig & Nesvorný (2015), Deienno et al. (2016, 2018), and Nesvorný et al. (2017).

present a depletion factor that is about an order of magnitude lower than the IMB. This difference implies that objects that formed in those subregions have a much larger chance of surviving in place. This is noteworthy, as it implies that these subregions are the ones most likely to host asteroids that are native to the MAB. The overall depletion factors listed in the last column of Table 1 (labeled MAB) can only be used to determine overall mass loss, provided that the initial distribution of solids was even in all MAB subregions. The MAB’s overall depletion values should not be used in any circumstance to evaluate size-dependent depletion, e.g., changes in the SFD. The reason is that objects of different sizes may populate specific MAB subregions, thus being more or less likely to be depleted.

#### 4. Results

We are interested in evaluating both the evolution and depletion of the MAB SFD as well as the number of objects with  $D > 500$  km ((4) Vesta-like) that would grow over time within the core of the MAB (see Section 3). Specifically, given the importance of knowing where an object of a certain size is in order to estimate the depletion effects (Table 1), we are interested in following the growth of these large objects within all five MAB subregions, i.e., EiMB, IMB, CMB, OMB, and EoMB (see Section 3 for the definition of such subregions). Still, for clarity and simplicity, the results reported in Sections 4.1, 4.2, and 4.3 are only presented with respect to the entire MAB and following our fiducial case (D18; Section 2, Table 1). A detailed breakdown of our results per MAB subregion while also following the C19 models can be found in the [Appendix](#).

##### 4.1. MAB Developed SFD

The current cumulative MAB SFD presents a very characteristic power slope in the  $100 \text{ km} < D < 500 \text{ km}$  range. As first pointed out by Bottke et al. (2005a) and later confirmed by Morbidelli et al. (2009), this cumulative SFD slope is a fossil of the MAB population post-gas-disk lifetime and necessary to reproduce the current “bump” observed near  $D = 100$  km (see also Section 4 in Deianno et al. 2022 for additional and similar discussion related to C-complex implanted planetesimals in the MAB). For that reason, an important sanity check is to confirm that the cumulative power slope of our evolved SFDs would, at the very least, reasonably resemble the current MAB SFD power slope in the same diameter range by the end of the gas disk lifetime.

In Figure 3, we present the evolved SFDs resulting from our simulations. The resultant SFDs for  $T = 3$  Myr (left panels (a) and (c)) and  $T = 5$  Myr (right panels (b) and (d)) are very similar. Therefore, having the gas dispersal time be 3 or 5 Myr produces only minor changes (also noted by Walsh & Levison 2019) and should not affect the overall growth and evolution of the early MAB. Some small differences are observed between simulations where we did not consider Jupiter’s influence (top panels (a) and (b)) and those where we did (bottom panels (c) and (d)). The main differences are in respect to the number and slope of the distribution for objects with  $D > 500$  km. The gravitational perturbation of Jupiter induces larger eccentricities in the MAB. This causes the collisions to become more erosive, which frustrates growth (e.g., Walsh & Levison 2019). Yet of greater importance for

this work’s analysis is the fact that all evolved SFDs look very similar within the shaded blue region. This means that the influence of Jupiter is not sufficient to change the slope of the MAB SFD for objects with  $100 \text{ km} < D < 500 \text{ km}$ .

The fact that our evolved SFDs preserve the primordial power-law slope of the cumulative distribution for objects with  $100 \text{ km} < D < 500 \text{ km}$  indicates that our simulations are compatible with the finds by Morbidelli et al. (2009) and the basic characteristics of the current MAB SFD. Thus, we can safely use our evolved SFDs to apply our depletion rates from Table 1 in order to determine what initial MAB mass (primordial mass that formed 0.5 Myr after CAIs; Section 2) can reproduce the current SFD, the number of objects with  $D > 500$  km, and the total mass observed in S-complex asteroids (dashed gray line in Figure 3; under the assumption that the S-complex component of the current MAB represents about one-fourth of the current MAB total mass, i.e., S-complex SFD =  $0.25 \times$  MAB SFD; Mothé-Diniz et al. 2003).

##### 4.2. MAB SFD after Uneven Depletion

As observed in Figure 3, all evolved SFDs are above the S-complex SFD line by a factor of a few to many. The goal of this section is to determine how the SFDs from Figure 3 would compare with the current S-complex SFD after applying the depletion factors presented in Table 1. It is important to notice, however, that a very large fraction of the S-complex SFD as defined at the end of the last section and presented in Figure 3 is composed of S-type asteroids (recall that we include all noncarbonaceous taxonomic classes, not just S-types, in our generic S-complex definition; e.g., DeMeo & Carry 2014). This is important information because S-type asteroids are believed to have formed from chondrules associated with the parent bodies of ordinary chondrites (Chapman 1996; Nakamura et al. 2011), which most likely formed within 2–3 Myr after CAIs (e.g., Pape et al. 2019). It may be thus slightly imprecise to directly compare our depleted SFDs with what we generically call the S-complex SFD. As planetesimals in our simulations are assumed to have formed 0.5 Myr after CAIs (Izidoro et al. 2022; Morbidelli et al. 2022), by  $T = 3$  or 5 Myr, they would most likely be differentiated objects (e.g., Lichtenberg et al. 2021) like asteroid (4) Vesta. Therefore, for consistency, one may argue that our evolved and depleted SFDs can only be compared to the SFD of differentiated MAB objects. However, it is also important to notice that our SFDs do not significantly evolve from 3 to 5 Myr (Figure 3). This leads to the conclusion that the late-formed (2–3 Myr after CAIs) S-type component of the SFD would only be affected by depletion via giant planet instability; i.e., it would not contribute to accretion. Once again, one may argue that for consistency, we should add a second population of asteroids (S-types) to that of our evolved SFDs. We cannot do that, however, because we have zero information on where (in which specific MAB subregion) large S-type bodies would form. As we will see below, as different MAB subregions have different depletion factors (Table 1), this makes SFD depletion size-dependent. Thus, assuming that larger late-formed S-types would populate one subregion over the other could lead to very misleading conclusions. Given all that discussion, we argue that the comparison between our results and our generically defined S-complex SFD is valid and correct. Therefore, we can safely assume that the overall evolved SFDs from Figure 3 would not change provided that (i)

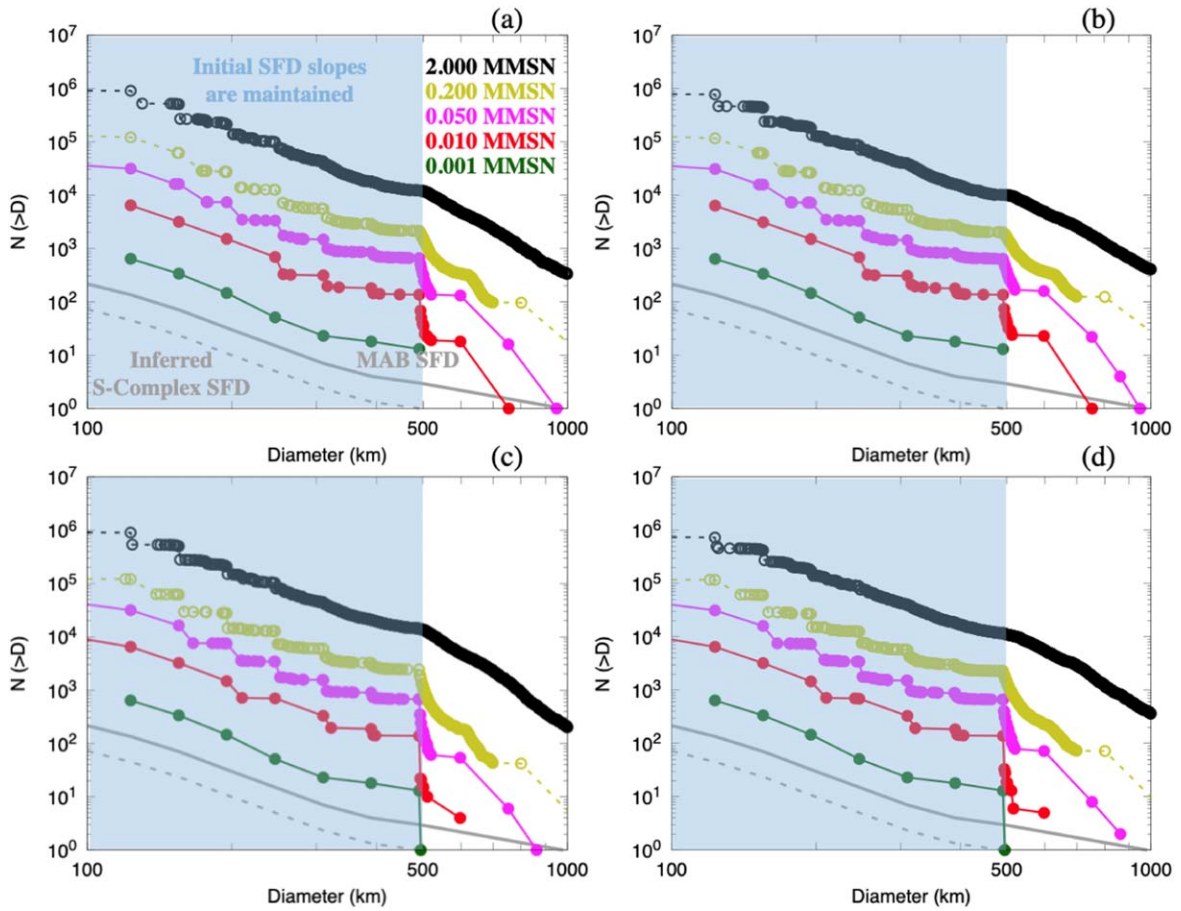


**Figure 3.** Evolved SFDs. Top panels ((a)  $T = 3$  Myr and (b)  $T = 5$  Myr) are for simulations where we did not consider Jupiter’s perturbation. Bottom panels ((c)  $T = 3$  Myr and (d)  $T = 5$  Myr) are for simulations where we considered Jupiter’s perturbation. For reference, we show (1) a solid gray line at the bottom representing the current MAB SFD from Bottke et al. (2005a) and (2) a dashed gray line representing our inferred SFD for S-complex asteroids (Mothé-Diniz et al. 2003; see main text.). Other colored symbols/lines are the same as in Figure 1, but only a few cases are highlighted to improve visualization. Those are (from top to bottom): 2.000 MMSN (black), 0.200 MMSN (yellow), 0.050 MMSN (magenta), 0.010 MMSN (red), and 0.001 MMSN (green). The shaded blue area indicates the target diameter range where the evolved SFD slope needs to resemble that of the current MAB SFD.

the population of late-formed S-type asteroids was not overwhelmingly large, and (ii) they formed with a cumulative SFD power slope in the range  $100 \text{ km} < D < 500 \text{ km}$ , similar to what we considered for our primordial population of planetesimals at 0.5 Myr. Both assumptions (i) and (ii) seem necessary to make our results compatible with the current-day observed MAB. As we will also show later in this section, these assumptions will, however, have larger implications for estimating the maximum amount of primordial MAB mass that formed in the MAB 0.5 Myr after CAIs.

It is important to also say that, in this work, we assume that our SFDs from Figure 3 would not change between the gas disk dispersal time and the onset of the giant planet instability. This is a reasonable approximation if we consider that the giant planet instability has to happen anytime within 100 Myr after gas disk dispersal (Nesvorný et al. 2018; Liu et al. 2022), and that collisional timescales can be of the order of or larger than that ( $t_{\text{coll}} \approx \mathcal{O}^8$  yr; Bottke et al. 2005a).

It is crucial to account for the semimajor axis dependency of depletion when attempting to glean insights into the nature of the primordial MAB from the current MAB SFD. Figure 4 shows results for the expected SFDs postdepletion by our fiducial case, D18  $D_{\text{fac}}$  (Table 1). As we presented in Section 3 and Table 1, the depletion factors are uneven throughout all MAB subregions. Therefore, the estimated postdepletion SFDs

were calculated by applying D18  $D_{\text{fac}}$  to the evolved SFDs from each one of the MAB subregions separately<sup>15</sup> and combining them after. This is necessary to account for the likelihood of objects being depleted in one MAB subregion over the other, which in the end makes depletion size- and semimajor-axis-dependent overall. For example, if 200  $D > 500 \text{ km}$  objects formed in the EiMB and IMB (100 in each subregion), accounting for D18  $D_{\text{fac}}$  for the MAB as a whole ( $200 \times 0.04553$ ) would lead to about nine survivors. On the other hand, if we apply the individual D18  $D_{\text{fac}}$  values for the EiMB and IMB,  $100 \times (0.000 + 0.0126)$ , the number of  $D > 500 \text{ km}$  survivors to be accounted for in the final MAB SFD would be one. That would lead to a completely different final SFD and conclusion. This is also the reason why we previously decided not to account for the contribution of late-formed S-types to our evolved SFDs while trying to guess, or assume, which MAB subregion they would populate. As larger objects ( $D \gtrsim 100 \text{ km}$  or so) are always less numerous than smaller kilometer-sized objects, depending on where they formed, uneven depletion may result in a steepening of the

<sup>15</sup> Following Deianno et al. (2022), we assume that depletion caused by the giant planet instability is overall size-independent within each independent MAB subregion. However, as depletion factors vary in each of the MAB subregions, the overall depletion by the giant planet instability may become size-dependent, as we illustrate in the main text.

depleted SFD when compared to its predepletion counterpart (e.g., see postdepletion slopes of yellow and blue SFDs in Figure 4 for  $D \gtrsim 200$  km). The above example clearly demonstrates the importance of considering the depletion factors per MAB subregion (especially when addressing size dependency) instead of the overall MAB depletion. The latter can only be used as a guide for the overall expected mass depletion.

With the postdepletion SFDs evaluated as in Figure 4, we can now use those results to estimate the maximum amount of primordial mass that could have ever existed in the MAB region at  $T = 0.5$  Myr. This maximum estimated primordial mass, however, will be sensitive to our generic definition of the S-complex taxonomy. This is because, as discussed at the beginning of this section, all of the SFDs presented in Figure 4 will be a combination of late-formed S-type asteroids and early-formed differentiated bodies. The former, within our definition of the core of the MAB, currently represents a total amount of mass equal to  $M_{S\text{-types}} \approx 3.15 \times 10^{-5} M_{\oplus}$ .<sup>16</sup> Table 2 presents how this total amount of S-type mass is currently distributed in the MAB by subregion (see Current/postdepletion row). The following rows in Table 2, denoted by Predepletion, show the expected amount of late-formed S-type mass in each MAB subregion from different models at 2–3 Myr after CAIs. Values presented in row Predepletion by D18, for instance, reflect our estimate once dividing the Current/postdepletion values by our fiducial D18  $D_{\text{fac}}$  numbers from Table 1 in each respective MAB subregion. These values represent the late-formed S-type mass (of a potential second population) that would need to be added to our primordial mass at 2–3 Myr but that would not contribute to subsequent SFD evolution by 3–5 Myr. Such an amount of mass would only be subject to depletion by the giant planet instability ( $D_{\text{fac}}$  values in Table 1). For each case (i.e., D18, C19<sub>all</sub>, and C19 <sub>$P_S/P_J$</sub> <sup>AMD<sub>JS</sub></sup>), the total amount of late-formed (Predepletion) S-type MAB mass (rightmost column in Table 2) was obtained by a simple sum of the numbers in each MAB subregion. We consider these values to be lower limits in the total S-type mass because  $D_{\text{fac}} = 0$  in the EiMB (Table 1) prevents us from estimating how many S-types could have ever formed in this specific subregion. Therefore, to avoid overestimating the total primordial MAB mass formed at  $T = 0.5$  Myr, the values we considered (Section 2) in our simulations should be decreased by the amounts shown in the rightmost column of Table 2.

Our results then indicate that, regardless of Jupiter’s inclusion and the exact timing of the nebula gas dispersal, while following our fiducial case, the current overall S-complex SFD (dashed line in Figure 4) can only be reproduced if the primordial MAB mass that formed 0.5 Myr after CAIs was of the order of or smaller than about  $\approx 2.14 \times 10^{-3} M_{\oplus}$  (i.e., 0.003  $M_{\oplus}$ , yellow in Figure 4, decreased by  $8.57 \times 10^{-4} M_{\oplus}$ ; Table 2). A total of  $2.14 \times 10^{-3} M_{\oplus}$  represents about 0.0016

MMSN following our methods in Section 2, which can still be approximated by 0.002 MMSN (yellow in Figure 4). Similarly, a potential upper limit (when considering values from C19<sub>all</sub> from Tables 1 and 2) on the primordial MAB mass should be somewhere between  $3.35 \times 10^{-3} M_{\oplus}$  and  $9.35 \times 10^{-3} M_{\oplus}$  (blue and red in Appendix Figure A1, i.e., 0.005 and 0.01 MMSN, respectively). Those upper limits in mass were obtained by subtracting  $3.65 \times 10^{-3} M_{\oplus}$  (Table 2) from 0.007 and 0.013  $M_{\oplus}$  (Section 2). Notably, a total of  $3.35 \times 10^{-3} M_{\oplus}$  represents about 0.0025 MMSN, which is very close to our estimate based on our fiducial parameters, whereas  $9.35 \times 10^{-3} M_{\oplus}$  represents about 0.0069 MMSN. However, we should reinforce that those depletion factors were derived by accounting for simulations in which Jupiter and Saturn’s angular momentum deficit (AMD) ended larger than 0.1 and/or their period ratio  $P_S/P_J$  exceeded 2.5. When not considering those extreme cases (see Appendix Figure A2 for a comparison), and applying C19 <sub>$P_S/P_J$</sub> <sup>AMD<sub>JS</sub></sup>, our results once again suggest that the current S-complex SFD can only be reproduced if the MAB primordial mass at  $T = 0.5$  Myr was of the order of or smaller than that represented by 0.002 MMSN (yellow in Appendix Figure A2). Interestingly enough, however, Table 2 values associated with C19 <sub>$P_S/P_J$</sub> <sup>AMD<sub>JS</sub></sup> suggest that the late-formed S-type mass at 2–3 Myr should be  $\gtrsim 4.48 \times 10^{-3} M_{\oplus}$ . Subtracting  $4.48 \times 10^{-3} M_{\oplus}$  of late-formed S-types from a potential primordial population of 0.003  $M_{\oplus}$  (i.e., 0.002 MMSN) that formed at 0.5 Myr would lead to a negative value. This would then imply that according to C19 <sub>$P_S/P_J$</sub> <sup>AMD<sub>JS</sub></sup>, the MAB should have necessarily formed devoid of mass (e.g., Raymond & Izidoro 2017b). Yet we caution for such a conclusion because, although the C19 <sub>$P_S/P_J$</sub> <sup>AMD<sub>JS</sub></sup> case is not as extreme as C19<sub>all</sub>, the final distribution of objects in each MAB subregion (C19 <sub>$P_S/P_J$</sub> <sup>AMD<sub>JS</sub></sup>  $N_{\text{ast}}^{\text{final}}$ ) compared to the MPC catalog (MPC  $N_{\text{ast}}$ ; Table 1) is not good. In fact, the high estimate of late-formed S-type mass of  $\gtrsim 4.48 \times 10^{-3} M_{\oplus}$  is mainly a result of C19 <sub>$P_S/P_J$</sub> <sup>AMD<sub>JS</sub></sup>  $D_{\text{fac}} = 0.239 \times 10^{-2}$  in the IMB (with only four asteroids surviving compared to 43 from MPC, a factor of  $>10$ ), which leads to a potentially misleading IMB predepletion mass of  $\approx 3.08 \times 10^{-3} M_{\oplus}$ . On the other hand, without knowing which subregion of the MAB those late-formed S-types would populate overall, we cannot take C19 <sub>$P_S/P_J$</sub> <sup>AMD<sub>JS</sub></sup> in a negative light. If, for example, most of the large estimated mass in the IMB is in a few large bodies (i.e., represented solely by the “unknown large diameter end” of the late-formed S-type SFD), even if some primordial mass existed in the IMB, all that is needed is that those few larger bodies are lost. This seems plausible when considering the differences in depletion rates for different MAB subregions (Table 1), and it further stresses the importance of considering size and semimajor axis dependency as we did in our analyses of Figure 4. Based on all the discussion from this paragraph, we conclude that it is reasonable to be conservative and solely rely on our fiducial estimates based on D18 from Deianno et al. (2018) for the lower limit of  $\gtrsim 8.57 \times 10^{-4} M_{\oplus}$  in late-formed S-type mass at around 2–3 Myr. This leads us to the conclusion that the primordial MAB S-complex mass at  $T = 0.5$  Myr after CAIs needs to be  $\lesssim 2.14 \times 10^{-3} M_{\oplus}$ .

We should once again stress that our estimate for the total MAB primordial mass (formed 0.5 Myr after CAIs) above is an upper limit. The reason is mostly because, in addition to all that was discussed in the previous paragraph, we cannot evaluate how much extra mass would be added to the S-complex MAB

<sup>16</sup> To estimate the total amount of S-type mass, we used information from <https://mp3c.oca.edu> via “Old Best Values” under the “Search” drop-down menu and following instructions included in the “Search by parameters” tab. We restricted our search to semimajor axes in the range  $1.9 \text{ au} < a < 3.6 \text{ au}$ ,  $0 < \sin(i) < 0.342$  ( $\approx 20^\circ$ ), and  $1.9 \text{ au} < q < 3.6 \text{ au}$ , while selecting “Spectral classes” as *S*, *Sq*, *Sk*, and *Sr* for S-types and excluding *Q*, *V*, *B*, *C*, *Cb*, *Ch*, *Cg*, *Cgh*, *X*, *Xk*, *Xc*, *Xe*, *E*, *M*, and *P* (which includes both C-complex and differentiated S-complex bodies; Delbo et al. 2019; see also Delbo et al. 2017; Delbo 2017). We also assumed a  $3 \text{ g cm}^{-3}$  density for all asteroids and only accounted for those with listed diameters larger than 0. However, we did not use these objects’ diameters when comparing with our evolved/depleted SFDs due to the potential effect of data incompleteness.

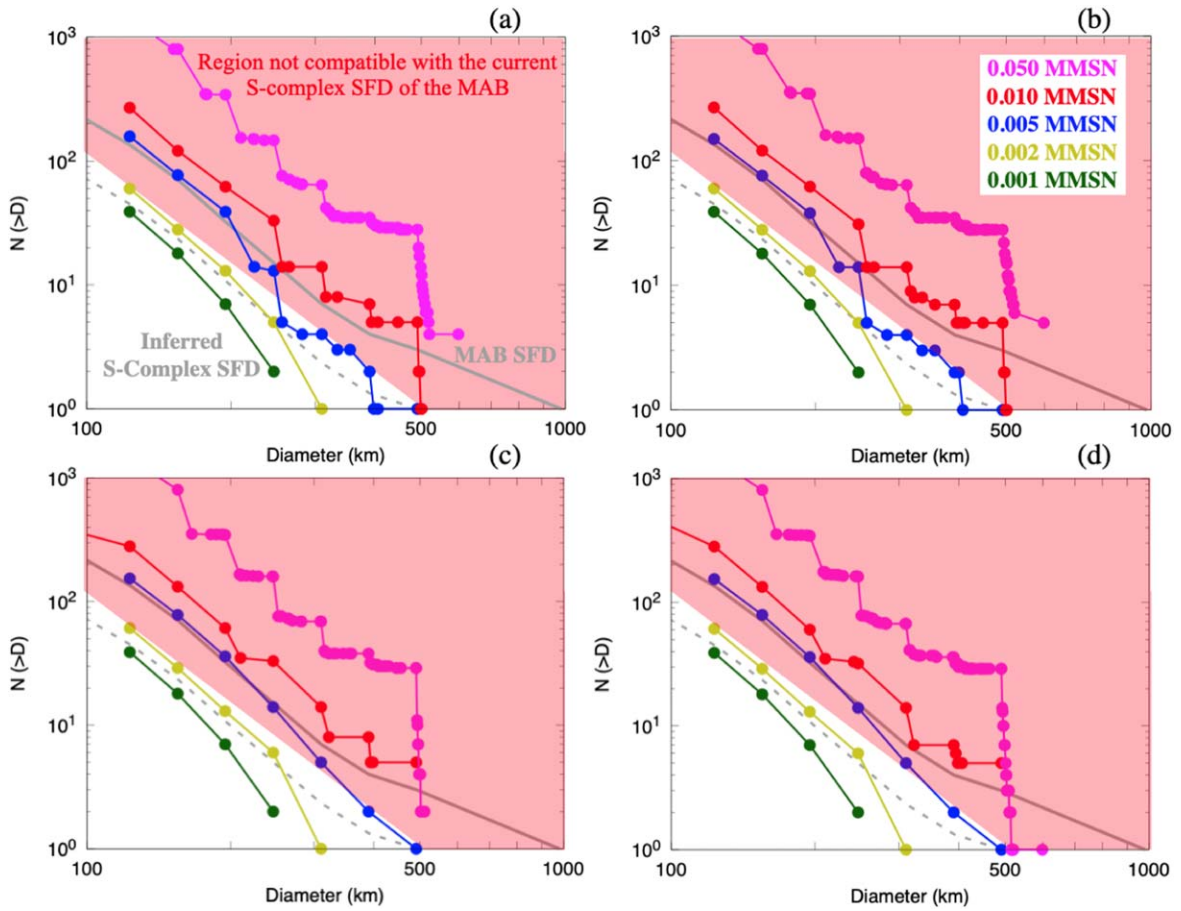


**Figure 4.** Expected SFDs after depletion following our fiducial parameters (D18  $D_{\text{fac}}$ ) on each individual MAB subregion. As in Figure 3, top panels ((a)  $T = 3$  Myr and (b)  $T = 5$  Myr) are for simulations where we did not consider Jupiter’s perturbation. Bottom panels ((c)  $T = 3$  Myr and (d)  $T = 5$  Myr) are for simulations where we considered Jupiter’s perturbation. For reference, we show (1) a solid gray line at the bottom representing the current MAB SFD from Bottke et al. (2005a) and (2) a dashed gray line representing our inferred SFD for S-complex asteroids (Mothe-Diniz et al. 2003; see Section 4.1.). Initial MMSN cases (primordial MAB masses at  $T = 0.5$  Myr) are represented by colors and symbols as in Figures 1 and 3 (labeled at the top right corner of panel (b)); not all cases are shown for clarity purposes): 0.050 MMSN (magenta), 0.010 MMSN (red), 0.005 MMSN (blue), 0.002 MMSN (yellow), and 0.001 MMSN (green). The red shaded area represents depleted SFDs that are not compatible with the current S-complex SFD (gray dashed line) and in most cases comparable to or even higher than the total MAB SFD (gray solid line).

**Table 2**  
Columns Represent the Estimated Amount of Mass in Each Different MAB Subregion (Section 3)

S-type Mass ( $M_{\oplus}$ )	EiMB	IMB	CMB	OMB	EoMB	MAB
Current/postdepletion	0.00	$7.37 \times 10^{-6}$	$1.85 \times 10^{-5}$	$5.50 \times 10^{-6}$	$9.40 \times 10^{-8}$	$\approx 3.15 \times 10^{-5}$
Predepletion by D18	...	$5.85 \times 10^{-4}$	$2.03 \times 10^{-4}$	$5.94 \times 10^{-5}$	$9.62 \times 10^{-6}$	$\gtrsim 8.57 \times 10^{-4}$
Predepletion by C19 <sub>all</sub>	0.00	$7.97 \times 10^{-4}$	$1.34 \times 10^{-3}$	$1.61 \times 10^{-4}$	$1.35 \times 10^{-3}$	$\approx 3.65 \times 10^{-3}$
Predepletion by C19 <sub><math>P_S/P_J^{\text{AMDJS}}</math></sub>	...	$3.08 \times 10^{-3}$	$9.95 \times 10^{-4}$	$5.15 \times 10^{-5}$	$3.52 \times 10^{-4}$	$\gtrsim 4.48 \times 10^{-3}$

**Note.** Current/postdepletion values were obtained following Delbo et al. (2019; see also Delbo et al. 2017; Delbo 2017). Predepletion values in each MAB individual subregion were evaluated by dividing Current/postdepletion values by D18, D19<sub>all</sub>, and D19 <sub>$P_S/P_J^{\text{AMDJS}}$</sub>   $D_{\text{fac}}$  from Table 1. The total Predepletion MAB S-type mass indicated in the last column of the three bottom lines is a simple sum of the respective columns on the left side. We do not report on Predepletion mass in the EiMB when  $D_{\text{fac}} = 0$ .

population via implantation during terrestrial planet growth (e.g., Raymond & Izidoro 2017b). Nonetheless, terrestrial planetesimals would probably be added to the MAB population after gas disk dispersal and would also not contribute to growth in the MAB. Their effective contribution to the shape of the S-complex SFD component is also unclear, and we leave this topic for future study. Yet the falloff (steepening) of our depleted SFDs for  $D \gtrsim 200\text{--}300$  km (Figure 4; e.g., yellow

curve) suggests that objects larger than those sizes, including the differentiated asteroid (4) Vesta, were likely terrestrial planetesimals implanted into the MAB (during terrestrial planet accretion; Raymond & Izidoro 2017b), rather than asteroids formed in situ at 0.5 Myr (the case of (4) Vesta) or at 2–3 Myr (the case of undifferentiated large objects) after CAIs.

Primordial MAB masses larger than about  $\approx 2.14 \times 10^{-3} M_{\oplus}$  formed 0.5 Myr after CAIs would generate SFDs incompatible

with our predicted S-complex SFD, unless depletion occurred much earlier than accretion could have taken place. However, although not shown, an analysis of the temporal evolution of our runs shows that the shape of the SFD as presented in Figure 3 for  $D > 500$  km objects develops within the first 0.5–1 Myr of evolution (i.e., similar to how we show that the shapes of the SFDs for  $T=3$  and 5 Myr do not change much; we could have shown it for any  $T \gtrsim 1$ –2 Myr). This indicates that accretion starts very early in cases where the MAB mass at 0.5 Myr is much larger than  $\approx 2.14 \times 10^{-3} M_{\oplus}$ . Knowing accretion starts very early, we can conclude that our results should be valid regardless of terrestrial planet formation model and/or early evolution of the giant planets (e.g., Walsh et al. 2011; Clement et al. 2018; Brož et al. 2021; Lykawka & Ito 2023). This is even less of a concern in the case of the works by Clement et al. (2018) and Lykawka & Ito (2023), as MAB depletion in those scenarios mostly occurs after gas disk dispersal, as we present here (i.e., long after accretion happened). Still, our results have larger consequences for those two works, as we discuss in the next paragraph.

Our low estimate for the primordial MAB mass points to the conclusion that there is no longer the need for an early giant planet instability to stunt Mars’ growth (Clement et al. 2018) or for chaotic dynamics to heavily deplete massive disk regions beyond 1–1.5 au (Lykawka & Ito 2023) after gas disk dispersal. We can confirm the latter. Our results demonstrate that there is no longer the need to heavily deplete a potentially primordial massive disk extending beyond 1–1.5 au. As we showed previously, such a disk likely never existed, or it would violate MAB constraints (i.e., SFD and number of (4) Vesta-like objects formed; Section 4.3). We find it difficult, however, from our results alone to explicitly rule out that an early giant planet instability occurring during terrestrial planet formation would not help in stunting Mars. We think that, depending on the initial profile of the planetesimal disk near 1–1.5 au (Izidoro et al. 2015, 2022; and whether or not growing embryos in that region would migrate due to interactions with the gas disk component; Brož et al. 2021; Woo et al. 2023), having an early giant planet instability occurring coincident with the later stages of terrestrial planet formation might still be a useful mechanism for preventing Mars from growing too large at 1.5 au (Nesvorný et al. 2021). Nonetheless, our work does reveal the necessity of, at the very least, revisiting the propositions by Clement et al. (2018) and Lykawka & Ito (2023). This is especially true if considering that most of their simulations that resulted in reasonable terrestrial planet analogs also depleted the MAB to levels that could potentially be incompatible with our new constraints.

#### 4.3. Growth of $D > 500$ km Objects and Their Depletion

The number of objects with  $D > 500$  km in the MAB and the particular subregion of the MAB where they reside are also important constraints. Knowing how many  $D > 500$  km objects formed and, more importantly, where they formed and survived depletion can be used as a further diagnostic for the maximum amount of mass that could have existed in the primordial MAB. The only known S-complex asteroid with  $D > 500$  km is (4) Vesta, (a V-type; DeMeo et al. 2009), which resides in the IMB. This is important information because very massive primordial MABs could lead to the formation of  $D > 500$  km objects in subregions as distant as the OMB, or even EoMB. Depletion factors are uneven, i.e., different in each MAB

subregion, and with higher survival chances in the CMB. That results in high probabilities of  $D > 500$  km objects surviving in subregions different than the IMB. In this section, we devote our attention to the specific problem of determining how many  $D > 500$  km objects formed in our simulations and in which subregion of the MAB they survived depletion.

Figure 5 shows the number of objects with  $D > 500$  km formed within the entire MAB region by  $T = 5$  Myr (blue triangles) as a function of the primordial MAB total mass in terms of MMSN fraction (Section 2) for a simulation where Jupiter is not present. Figure 5 also reports on the expected number of objects after depletion due to effects of the giant planet instability (Nesvorný & Morbidelli 2012; Deianno et al. 2017) and chaotic diffusion over 4.5 Gyr of solar system evolution (Minton & Malhotra 2010; Deianno et al. 2016, 2018, 2020), i.e., once applying our fiducial depletion factors from D18  $D_{\text{fac}}$  (green triangles) from Table 1. For simplicity, we do not show figures in this section with results for the cases where we considered Jupiter or  $T = 3$  Myr. A breakdown of those results, along with those for the C19  $D_{\text{fac}}$  cases, can be found in Appendix Tables A1 and A4.

The yellow shaded region in Figure 5 represents the acceptable number of  $D > 500$  km objects to survive in the MAB or, more specifically, the IMB after depletion ( $N \leq 1$ ). This number is considered assuming that the initial population of the MAB planetesimals would be of S-complex taxonomic classification (see discussion in Section 1). In this case, only asteroid (4) Vesta should be considered as an object of possible formation and survival within the IMB in our study, i.e.,  $N = 1$ . Still, we report on  $N \leq 1$ , i.e.,  $N = 0$  is a valid result, to account for the possibility where either no objects with  $D > 500$  km formed, or they formed but did not survive depletion. In this case, (4) Vesta would not be an object that originated in the MAB (or IMB, to be more specific; see Figure 2) but rather an object that formed in the terrestrial planet region and was later implanted into the IMB during terrestrial planet accretion (Raymond & Izidoro 2017b). We do not consider  $N = 2$  or 3 as an at least marginally successful outcome for two main reasons. First, although the existence of Vesta-like fragments (basaltic objects with V-type taxonomy) that do not show a direct orbital link to (4) Vesta and its family suggest the existence of other V-type parent bodies (e.g., Brasil et al. 2017; Burbine et al. 2023; Troianskyi et al. 2023), we have no information about their possible origin and size. Therefore, these hypothetical additional V-type parent bodies could likely be much smaller than our  $D = 500$  km size limit. This claim is supported by the absence of a second large and well-defined V-type family in the MAB. Second, we recall that (4) Vesta orbits in the IMB, and as we can see from Figure 5, the formation of a large number of  $D > 500$  km objects would likely lead to their survival in the CMB and OMB.

An analysis of Figure 5, as well as Appendix Tables A1 and A2, shows that a massive primordial MAB,  $M_{\text{disk}} \gtrsim 0.007$ – $0.013 M_{\oplus}$  (0.005–0.01 MMSN), leads to the formation of too many  $D > 500$  km objects. As some of them are likely to survive solar system evolution, this would imply that the current MAB should have not only the asteroid (4) Vesta but other larger S-complex asteroids. Furthermore, a very large number of these large objects would reside in subregions other than the IMB if the primordial MAB mass was larger than about  $0.003 M_{\oplus}$  (or, more specifically,  $\approx 2.14 \times 10^{-3} M_{\oplus}$ , Section 4.2, a direct consequence of uneven depletion). This

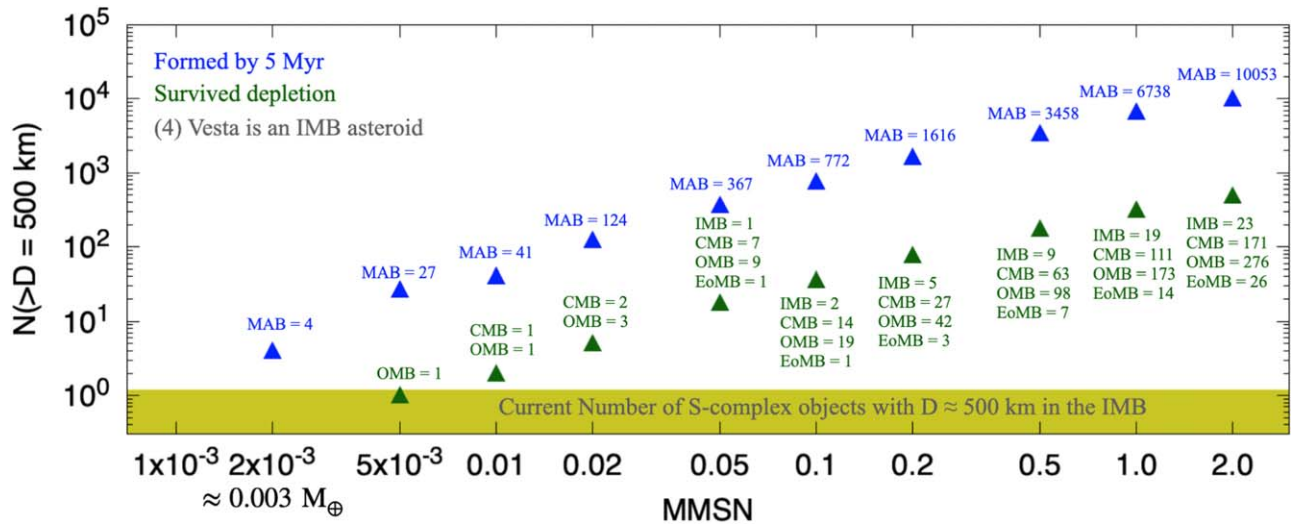


**Figure 5.** Number of objects with  $D > 500$  km formed within the entire MAB region by  $T = 5$  Myr (blue triangles) as a function of the primordial MAB total mass in terms of MMSN fraction (Section 2) in a simulation where Jupiter was not present. Blue labels on top of blue triangles show the exact number of objects formed. These numbers are obtained by summing the number of all objects with  $D > 500$  km formed in all five MAB subregions defined in Section 3, i.e., EiMB, IMB, CMB, OMB, and EoMB. Green triangles refer to the expected number of  $D > 500$  km objects that would survive solar system evolution after gas nebula dispersal when applying our fiducial D18  $D_{\text{fac}}$  depletion factors (Table 1). Green labels on top of green triangles show how many survived depletion and in which MAB subregion (see Appendix Table A1 at  $T = 5$  Myr). The yellow shaded region represents the acceptable number of  $D > 500$  km objects to survive in the IMB after depletion (see main text).

result strengthens our conclusion from previous sections in that the MAB primordial mass (at  $T = 0.5$  Myr after CAIs) should be smaller than about  $\approx 2.14 \times 10^{-3} M_{\oplus}$  or somehow depleted to this level before accretion starts.

Comparing Appendix Tables A1 and A2, we find that the presence of Jupiter systematically leads to the formation of fewer such large objects, especially within the OMB and EoMB, but also within the CMB. As anticipated in Section 4.1, this is because Jupiter strongly perturbs the subregions from the OMB to EoMB (and partially the CMB), causing the orbital eccentricity of objects in those subregions to increase. A direct consequence of this eccentricity excitation is that collision velocities among growing objects increase, leading to fragmentation and preventing further growth (e.g., Walsh & Levison 2019). The same effect also explains why depletion seems more aggressive in cases with Jupiter (e.g., compare the number within parentheses in both Appendix Tables A1 and A2 for every case). This is because, when Jupiter is considered,  $D > 500$  km objects are more likely to form only within the EiMB, IMB, and CMB, with the large majority populating the first two subregions. Depletion factors associated with the EiMB and IMB are much larger than the ones for the CMB (Table 1). This further strengthens our claim that it is very important to account for depletion in each different MAB subregion separately instead of using the overall depletion factor as a proxy for size-dependent depletion.

## 5. Conclusions

The primary goal of our work was to determine the maximum possible total mass that could have existed in the primordial MAB region. The current MAB total mass is tiny ( $\approx 5 \times 10^{-4} M_{\oplus}$ ; DeMeo & Carry 2014). There is a debate in the literature on whether such a small MAB mass was primordial (e.g., Hansen 2009; Levison et al. 2015a; Izidoro et al. 2015, 2021; Deianno et al. 2016, 2018) or whether the primordial MAB total mass was much larger than currently

observed (e.g., Walsh et al. 2011; Clement et al. 2019; Lykawka & Ito 2023).

In this work, we followed accretion (growth and fragmentation) of planetesimals in the MAB during the period when gas still existed in the solar nebula. We assumed different values of total mass for our primordial MAB (see Section 2 for a detailed description of model parameters) and that all of our primordial MAB asteroids would be of the inner solar system S-complex taxonomic type (DeMeo & Carry 2014); see also discussion in Section 1. We also attributed an SFD for the MAB primordial population as proposed by previous works that succeeded in reproducing the shape of the current MAB SFD (Bottke et al. 2005a; Morbidelli et al. 2009) but with limited dynamical effects. In our work, accretion was followed with the code LIPAD (Levison et al. 2012), meaning that we can in this work self-consistently follow dynamical and collisional evolution altogether. We studied cases where we considered the gravitational perturbation of Jupiter, as well as cases where we did not. The total simulation time was 5 Myr, i.e., presumably the time when gas in the solar nebula dispersed around the MAB region (based on the ages of the youngest CB chondrites, as well as on paleomagnetism constraints; Krot et al. 2005; Weiss et al. 2021). Our results confirm previous findings that the power slope of the MAB SFD does not change in the range  $100 \text{ km} < D < 500 \text{ km}$  (Bottke et al. 2005a; Morbidelli et al. 2009), which implies that such a slope should be primordial. This conclusion is true regardless of considering or not the effects of gravitational perturbation of Jupiter (see Section 4.1).

After following how the MAB SFD evolves under the above circumstances, we considered how the MAB population would be depleted during subsequent solar system evolution. This is important, as it is well known that the giant planet instability (Nesvorný & Morbidelli 2012; Deianno et al. 2017), predicted to have happened some time after gas disk dispersal, inevitably depletes MAB objects (Roig & Nesvorný 2015; Deianno et al.

2016, 2018; Nesvorný et al. 2017; Clement et al. 2019). It is also well known that an additional factor of 2 in depletion is expected due to chaotic diffusion of MAB objects leaking through MMRs over Gyr timescales (Minton & Malhotra 2010). We used results from the literature (e.g., Deianno et al. 2018; Clement et al. 2019) to estimate depletion factors that would account for both the giant planet instability and subsequent chaotic diffusion. To do that, we first reduced the data from these works to the same standards. Then, we subdivided the MAB into five subregions, i.e., the EiMB, IMB, CMB, OMB, and EoMB (see Section 3 for a definition of these subregions and a detailed description of MAB limits and data reduction). Finally, we compared our findings with data from real asteroids in the MPC catalog.

The first main result of the present work is that we found that the MAB depletion is uneven; i.e., different radial subregions of the MAB are depleted at different rates (Table 1). This important result was first suggested by Nesvorný et al. (2017) but never quantified in detail. Here we demonstrate that the CMB and OMB have a much higher survival rate (lower depletion rates) than any other subregion. This is noteworthy, as it implies that these subregions are the ones most likely to host asteroids that are native to the MAB. Our results, as shown in Sections 4.2 and 4.3, clearly demonstrate how such uneven MAB depletion becomes size- and semimajor-axis-dependent. For that reason, we suggest that follow-up works use the values for each MAB subregion derived in Table 1 separately when accessing depletion of the MAB in a similar way as performed in this work. The overall MAB depletion factor reported in the last column of Table 1 should only be used as a guide for estimating overall mass depletion, but not size-dependent population depletion, as the latter is also semimajor-axis-dependent.

The second main result of the present work is that we found that the maximum total mass that could have formed in the primordial MAB around 0.5 Myr after CAIs is likely to be smaller than  $\approx 2.14 \times 10^{-3} M_{\oplus}$ . Primordial MAB masses larger than this limit would unavoidably lead to the development of SFDs inconsistent with the current inferred SFD for S-complex asteroids (Mothé-Diniz et al. 2003). Such larger primordial MAB masses would also likely lead to the formation of too many S-complex objects with  $D > 500$  km. Our depletion factors as presented in Table 1 and following the methods and rationale described in Sections 4.2 and 4.3 indicate that most objects of this size would survive in the CMB and OMB. Given that the only S-complex object with  $D > 500$  km ((4) Vesta) resides in the IMB, we consider such results to be incompatible with observations. Furthermore, we find that objects with  $D > 200$ –300 km, including asteroid (4) Vesta, are more likely

to be terrestrial planetesimals implanted into the MAB (or, more specifically, into the IMB) during terrestrial planet growth (Raymond & Izidoro 2017b) rather than asteroids that grew in situ (see discussion in Sections 4.2 and 4.3 for a detailed rationale).

Finally, we conclude by noting that our results are independent of terrestrial planet formation models and/or early evolution of the giant planets (e.g., Walsh et al. 2011; Clement et al. 2018; Brož et al. 2021; Lykawka & Ito 2023). This conclusion is supported by the fact that, for primordial MAB masses larger than  $\approx 2.14 \times 10^{-3} M_{\oplus}$ , accretion into the MAB starts very early (i.e., within the first few hundred kyr after planetesimal formation, here considered to be 0.5 Myr after CAIs; Lichtenberg et al. 2021; Izidoro et al. 2022; Morbidelli et al. 2022). However, most of the MAB depletion happens after gas disk dispersal via a giant planet instability (e.g., Deianno et al. 2018; Clement et al. 2019) or chaotic excitation induced by secular resonance sweeping (Izidoro et al. 2016; Lykawka & Ito 2023). Therefore, unless depletion took place within the first few hundred kyr after CAIs, MAB primordial masses larger than  $\approx 2.14 \times 10^{-3} M_{\oplus}$  would lead to unobserved features in the current MAB. Such early depletion seems unlikely even in such models as those proposed by Walsh et al. (2011) and Brož et al. (2021).

### Acknowledgments

We thank the two anonymous reviewers for their positive and constructive comments that helped improve our work. The work of R.D. and K.J.W. was supported by the NASA Emerging Worlds program, grant 80NSSC21K0387. D.N.'s work was supported by the NASA Emerging Worlds program. M.S.C. is supported by NASA Emerging Worlds grant 80NSSC23K0868 and NASA's CHAMPs team, supported by NASA under grant No. 80NSSC21K0905 issued through the Interdisciplinary Consortia for Astrobiology Research (ICAR) program. W.F.B.'s work in this paper was supported by NASA's Psyche mission through contract NNM16AA09C.

### Appendix

For clarity and simplicity, results reported in Sections 4.1, 4.2, and 4.3 were presented mostly with respect to the entire MAB while following our fiducial case (D18; Section 2, Table 1). In this appendix we present a detailed breakdown of our results per MAB subregion while also following C19 models. We present our expected postdepletion MAB SFDs based on C19 models in Figures A1 and A2. Tables A1 and A2 show a detailed breakdown of our results per MAB subregions.

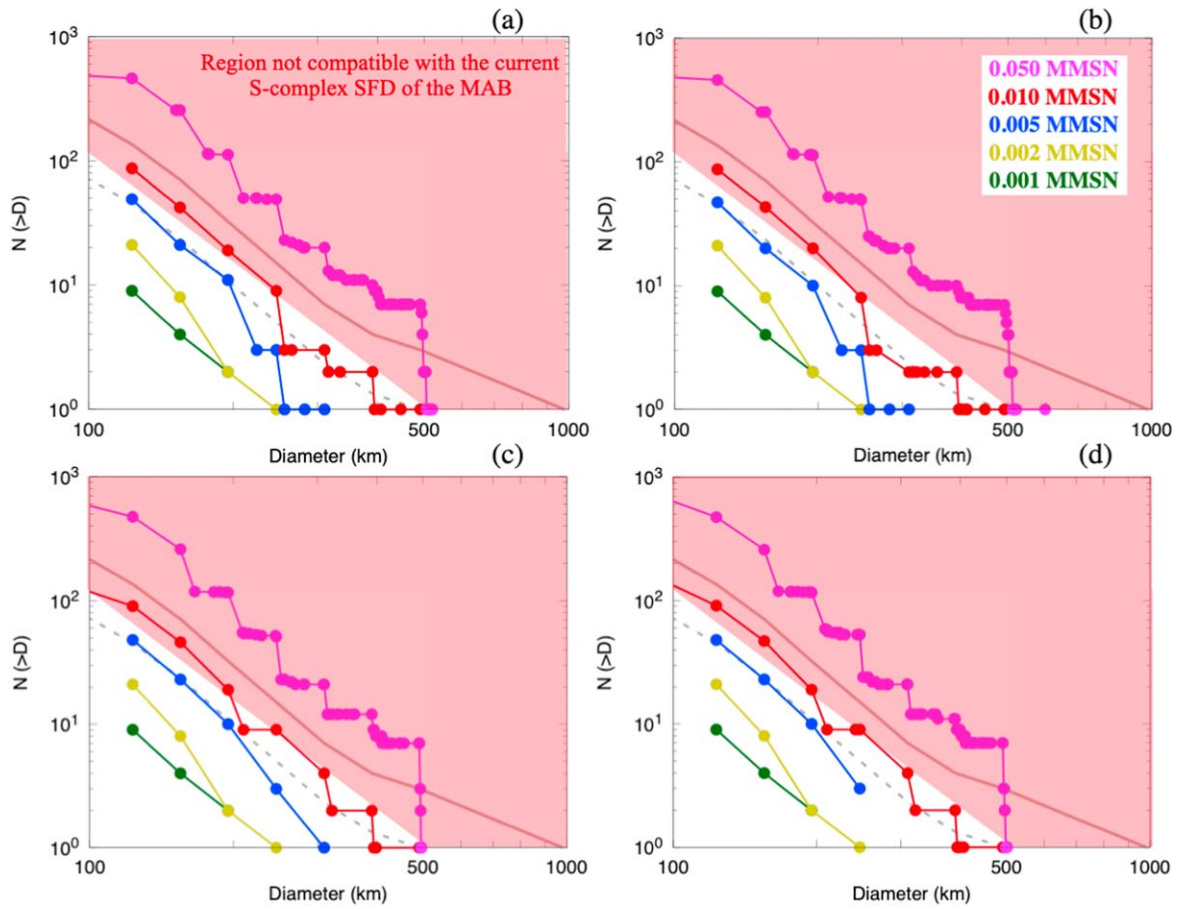


**Figure A1.** Same as Figure 4, but considering the potential upper limit depletion case from C19<sub>all</sub> from Table 1, i.e., where we did not exclude cases in which Jupiter and Saturn's AMD ended larger than 0.1 and/or their period ratio  $P_S/P_J$  exceeds 2.5 (see Figure A2 below for a comparison).

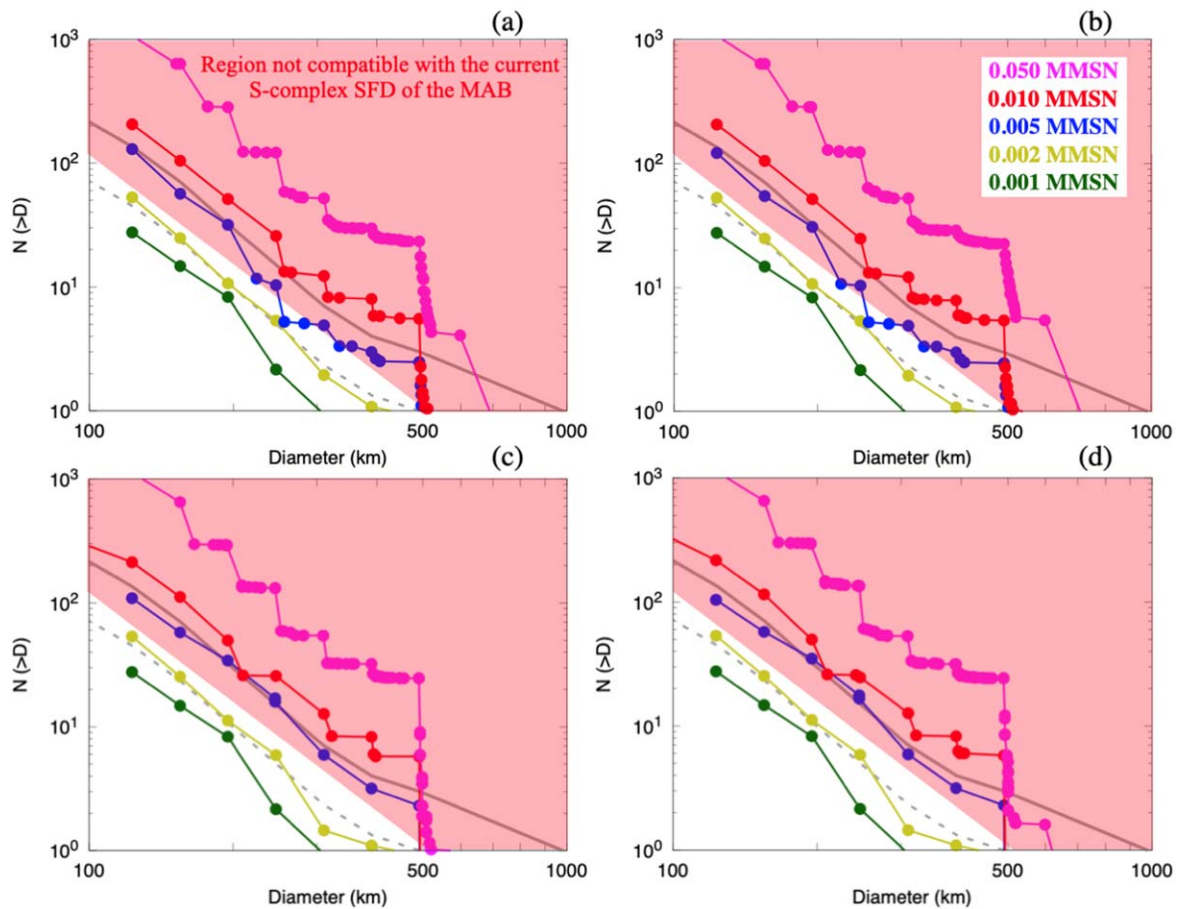


**Figure A2.** Same as Figures 4 and A2, while applying the depletion factor from  $C19_{P_S/P_J}^{AMD_{J_S}}$  from Table 1, i.e., only considering cases from Clement et al. (2019) where Jupiter and Saturn’s AMD remained lower than 0.1 and their period ratio did not exceed 2.5 (similar to cases from Roig & Nesvorný 2015; Deianno et al. 2016, 2018; Nesvorný et al. 2017; D18  $D_{fac}$  in Table 1).

**Table A1**

Number of  $D > 500$  km Objects Formed at  $T = 3$  and 5 Myr Followed by the Expected Number of Survivors after Applying ( $D18/C19_{all}/C19_{P_S/P_J}^{AMD_{J_S}} D_{fac}$ ) while *Not* Considering Jupiter

$T = 3$ Myr						
MMSN (1)	EiMB (2)	IMB (3)	CMB (4)	OMB (5)	EoMB (6)	MAB (7)
0.001	0 (0/0/0)	0 (0/0/0)	0 (0/0/0)	0 (0/0/0)	0 (0/0/0)	0 (0/0/0)
0.002	0 (0/0/0)	2 (0/0/0)	1 (0/0/0)	1 (0/0/0)	0 (0/0/0)	4 (0/0/0)
0.005	4 (0/0/0)	3 (0/0/0)	2 (0/0/0)	8 (1/0/1)	8 (0/0/0)	25 (1/0/1)
0.010	2 (0/0/0)	9 (0/0/0)	11 (1/0/0)	8 (1/0/1)	6 (0/0/0)	36 (2/0/1)
0.020	15 (0/0/0)	27 (0/0/0)	12 (1/0/0)	26 (2/1/3)	23 (0/0/1)	103 (3/1/4)
0.050	42 (0/0/0)	65 (1/1/0)	63 (6/1/1)	83 (8/3/9)	55 (1/0/1)	308 (16/5/11)
0.100	95 (0/0/0)	169 (2/2/0)	128 (12/2/2)	173 (16/6/18)	118 (1/1/3)	683 (31/11/23)
0.200	174 (0/1/0)	395 (5/4/1)	279 (25/4/5)	399 (37/14/42)	263 (3/2/7)	1510 (70/25/55)
0.500	378 (0/1/0)	746 (9/7/2)	811 (74/11/15)	1101 (102/38/117)	747 (7/5/20)	3783 (192/62/154)
1.000	723 (0/2/0)	1609 (20/15/4)	1485 (135/20/28)	1870 (173/64/198)	1639 (16/11/44)	7326 (344/112/274)
2.000	865 (0/3/0)	2244 (28/21/5)	2101 (192/29/39)	3528 (326/121/373)	3073 (30/21/82)	11811 (576/195/499)
$T = 5$ Myr						
0.001	0 (0/0/0)	0 (0/0/0)	0 (0/0/0)	0 (0/0/0)	0 (0/0/0)	0 (0/0/0)

**Table A1**  
(Continued)

<b><math>T = 5</math> Myr</b>						
0.002	0 (0/0/0)	2 (0/0/0)	1 (0/0/0)	1 (0/0/0)	0 (0/0/0)	4 (0/0/0)
0.005	5 (0/0/0)	3 (0/0/0)	3 (0/0/0)	8 (1/0/1)	8 (0/0/0)	27 (1/0/1)
0.010	3 (0/0/0)	11 (0/0/0)	11 (1/0/0)	9 (1/0/1)	7 (0/0/0)	41 (2/0/1)
0.020	14 (0/0/0)	31 (0/0/0)	17 (2/0/0)	35 (3/1/4)	27 (0/0/1)	124 (5/1/5)
0.050	46 (0/0/0)	88 (1/1/0)	74 (7/1/1)	92 (9/3/10)	67 (1/0/2)	367 (18/5/13)
0.100	95 (0/0/0)	196 (2/2/0)	151 (14/2/3)	200 (19/7/21)	130 (1/1/3)	772 (36/12/27)
0.200	178 (0/1/0)	404 (5/4/1)	291 (27/4/5)	450 (42/15/48)	293 (3/2/8)	1616 (77/26/62)
0.500	327 (0/1/0)	708 (9/7/2)	692 (63/10/13)	1059 (98/36/112)	672 (7/5/18)	3458 (177/59/145)
1.000	651 (0/2/0)	1518 (19/14/4)	1219 (111/17/23)	1869 (173/64/198)	1481 (14/10/40)	6738 (317/107/265)
2.000	660 (0/2/0)	1861 (23/17/4)	1881 (171/26/35)	2982 (276/102/316)	2669 (26/19/71)	10053 (496/166/426)

**Note.** Detailed information showing the exact number of objects with  $D > 500$  km that formed in each of the five individual MAB subregion (columns (2)–(6), number outside parentheses; see Sections 1 and 2 for definitions), as well as in the entire MAB (last column; values plotted in Figure 5 on top of blue triangles at  $T = 5$  Myr). We also present the expected survival of all  $D > 500$  km objects formed after applying the depletion factors from Deianno et al. (2018) and Clement et al. (2019) using values from Table 1 in the format (D18/C19<sub>all</sub>/C19<sub>PS/P<sub>J</sub></sub><sup>AMD<sub>J<sub>S</sub></sub></sup>  $D_{\text{fac}}$ ). Boldface values from D18  $D_{\text{fac}}$  at  $T = 5$  Myr are those plotted in green in Figure 5. Results are shown for all MMSN (first column) and for the case where Jupiter was **not** present in the simulations, at  $T = 3$  (top rows) and 5 Myr (bottom rows; recall that our simulations start at  $T = 0.5$  Myr once we considered planetesimals formed by this time after CAIs; Lichtenberg et al. 2021; Izidoro et al. 2022; Morbidelli et al. 2022).

**Table A2**

Number of  $D > 500$  km Objects Formed at  $T = 3$  and 5 Myr Followed by the Expected Number of Survivors after Applying (D18/C19<sub>all</sub>/C19<sub>PS/P<sub>J</sub></sub><sup>AMD<sub>J<sub>S</sub></sub></sup>  $D_{\text{fac}}$ ) when Jupiter Is Considered in the Simulation.

<b><math>T = 3</math> Myr</b>						
MMSN (1)	EiMB (2)	IMB (3)	CMB (4)	OMB (5)	EoMB (6)	MAB (7)
0.001	0 (0/0/0)	0 (0/0/0)	0 (0/0/0)	0 (0/0/0)	0 (0/0/0)	0 (0/0/0)
0.002	0 (0/0/0)	0 (0/0/0)	0 (0/0/0)	1 (0/0/0)	1 (0/0/0)	2 (0/0/0)
0.005	0 (0/0/0)	1 (0/0/0)	1 (0/0/0)	0 (0/0/0)	1 (0/0/0)	3 (0/0/0)
0.010	3 (0/0/0)	10 (0/0/0)	3 (0/0/0)	0 (0/0/0)	0 (0/0/0)	16 (0/0/0)
0.020	11 (0/0/0)	14 (0/0/0)	3 (0/0/0)	4 (0/0/0)	2 (0/0/0)	34 (0/0/0)
0.050	32 (0/0/0)	69 (1/1/0)	24 (2/0/0)	22 (2/1/2)	18 (0/0/0)	165 (5/2/2)
0.100	97 (0/0/0)	153 (2/1/0)	81 (7/1/2)	101 (9/3/11)	47 (0/0/1)	479 (18/5/14)
0.200	195 (0/1/0)	373 (5/3/1)	201 (18/3/4)	246 (23/8/26)	131 (1/1/3)	1146 (47/16/34)
0.500	404 (0/1/0)	910 (11/8/2)	840 (77/12/16)	1094 (101/37/116)	587 (6/4/16)	3835 (195/62/150)
1.000	691 (0/2/0)	1624 (20/15/4)	1838 (168/25/34)	2359 (218/81/250)	1331 (13/9/36)	7843 (419/132/324)
2.000	1069 (0/3/0)	2319 (29/21/6)	2629 (240/36/49)	5084 (470/174/538)	2514 (25/18/67)	13615 (764/252/660)
<b><math>T = 5</math> Myr</b>						
0.001	0 (0/0/0)	0 (0/0/0)	0 (0/0/0)	0 (0/0/0)	0 (0/0/0)	0 (0/0/0)
0.002	0 (0/0/0)	0 (0/0/0)	0 (0/0/0)	1 (0/0/0)	1 (0/0/0)	2 (0/0/0)
0.005	0 (0/0/0)	1 (0/0/0)	1 (0/0/0)	0 (0/0/0)	1 (0/0/0)	3 (0/0/0)

**Table A2**  
(Continued)

$T = 5 \text{ Myr}$						
0.010	3 (0/0/0)	10 (0/0/0)	3 (0/0/0)	2 (0/0/0)	1 (0/0/0)	19 (0/0/0)
0.020	12 (0/0/0)	22 (0/0/0)	7 (1/0/0)	7 (1/0/1)	2 (0/0/0)	50 (2/0/1)
0.050	48 (0/0/0)	75 (1/1/0)	31 (3/0/1)	35 (3/1/4)	26 (0/0/1)	215 (7/2/6)
0.100	108 (0/0/0)	204 (3/2/0)	98 (9/1/2)	144 (13/5/15)	71 (1/0/2)	625 (26/8/19)
0.200	208 (0/1/0)	379 (5/4/1)	251 (23/3/5)	348 (32/12/37)	193 (2/1/5)	1379 (62/21/48)
0.500	326 (0/1/0)	815 (10/8/2)	881 (80/12/16)	1141 (106/39/121)	739 (7/5/20)	3902 (203/65/159)
1.000	671 (0/2/0)	1444 (18/13/3)	1624 (148/22/30)	2243 (207/77/237)	1424 (14/10/38)	7406 (387/124/308)
2.000	805 (0/3/0)	1981 (25/18/5)	2202 (201/30/41)	3847 (356/131/407)	2212 (22/15/59)	11047 (604/197/512)

**Note.** Detailed information showing the exact number of objects with  $D > 500 \text{ km}$  that formed in each of the five individual MAB subregion (columns (2)–(6), number outside parentheses; see Sections 1 and 2 for definitions), as well as in the entire MAB (last column). We also present the expected survival of all  $D > 500 \text{ km}$  objects formed after applying the depletion factors from Deienno et al. (2018) and Clement et al. (2019) using values from Table 1 in the format (D18/C19<sub>all</sub>/C19<sub>AMD<sub>J</sub>S</sub><sub>PS/P<sub>J</sub></sub>  $D_{\text{fac}}$ ). Boldface values are for results once applying D18  $D_{\text{fac}}$ . Results are shown for all MMSN (first column) and for the case when Jupiter is present in the simulations, at  $T = 3$  (top rows) and 5 Myr (bottom rows; recall that our simulations start at  $T = 0.5 \text{ Myr}$  once we considered planetesimals formed by this time after CAIs; Lichtenberg et al. 2021; Izidoro et al. 2022; Morbidelli et al. 2022).

### ORCID iDs

Rogério Deienno  <https://orcid.org/0000-0001-6730-7857>

David Nesvorný  <https://orcid.org/0000-0002-4547-4301>

Matthew S. Clement  <https://orcid.org/0000-0001-8933-6878>

William F. Bottke  <https://orcid.org/0000-0002-1804-7814>

André Izidoro  <https://orcid.org/0000-0003-1878-0634>

Kevin J. Walsh  <https://orcid.org/0000-0002-0906-1761>

### References

- Andrews, S. M., Wilner, D. J., Hughes, A. M., Qi, C., & Dullemond, C. P. 2010, *ApJ*, 723, 1241
- Andrews, S. M., Huang, J., Pérez, L. M., et al. 2018, *ApJL*, 869, L41
- Benz, W., & Asphaug, E. 1999, *Icar*, 142, 5
- Bitsch, B., Johansen, A., Lambrechts, M., & Morbidelli, A. 2015a, *A&A*, 575, A28
- Bitsch, B., Lambrechts, M., & Johansen, A. 2015b, *A&A*, 582, A112
- Bollard, J., Connelly, J. N., Whitehouse, M. J., et al. 2017, *SciA*, 3, e1700407
- Bottke, W. F., Durda, D. D., Nesvorný, D., et al. 2005a, *Icar*, 175, 111
- Bottke, W. F., Durda, D. D., Nesvorný, D., et al. 2005b, *Icar*, 179, 63
- Bottke, W. F., Vokrouhlický, D., Ballouz, R. L., et al. 2020, *AJ*, 160, 14
- Bottke, W. F., Vokrouhlický, D., Minton, D., et al. 2012, *Natur*, 485, 78
- Brasil, P. I. O., Roig, F., Nesvorný, D., & Carruba, V. 2017, *MNRAS*, 468, 1236
- Brasser, R., & Mojzsis, S. J. 2020, *NatAs*, 4, 492
- Brož, M., Chrenko, O., Nesvorný, D., & Dauphas, N. 2021, *NatAs*, 5, 898
- Burbine, T. H., Greenwood, R. C., Zhang, B., & Buchanan, P. C. 2023, *LPICo*, 2806, 2347
- Burbine, T. H., McCoy, T. J., Meibom, A., Gladman, B., & Keil, K. 2002, in *Asteroids III*, ed. W. F. Bottke, Jr. et al. (Tucson, AZ: Univ. Arizona Press), 653
- Burkhardt, C., Spitzer, F., Morbidelli, A., et al. 2021, *SciA*, 7, eabj7601
- Chambers, J. 2021, *ApJ*, 914, 102
- Chambers, J. E. 2001, *Icar*, 152, 205
- Chapman, C. R. 1996, *M&PS*, 31, 699
- Che, S., & Zega, T. J. 2023, *NatAs*, 7, 1063
- Clement, M. S., Deienno, R., Kaib, N. A., et al. 2021a, *Icar*, 367, 114556
- Clement, M. S., Kaib, N. A., Raymond, S. N., & Walsh, K. J. 2018, *Icar*, 311, 340
- Clement, M. S., Morbidelli, A., Raymond, S. N., & Kaib, N. A. 2020, *MNRAS*, 492, L56
- Clement, M. S., Raymond, S. N., & Kaib, N. A. 2019, *AJ*, 157, 38
- Clement, M. S., Raymond, S. N., Kaib, N. A., et al. 2021b, *Icar*, 355, 114122
- de Sanctis, M. C., Ammannito, E., Raponi, A., et al. 2015, *Natur*, 528, 241
- Deienno, R., Gomes, R. S., Walsh, K. J., Morbidelli, A., & Nesvorný, D. 2016, *Icar*, 272, 114
- Deienno, R., Izidoro, A., Morbidelli, A., Nesvorný, D., & Bottke, W. F. 2022, *ApJL*, 936, L24
- Deienno, R., Izidoro, A., Morbidelli, A., et al. 2018, *ApJ*, 864, 50
- Deienno, R., Morbidelli, A., Gomes, R. S., & Nesvorný, D. 2017, *AJ*, 153, 153
- Deienno, R., Nesvorný, D., Vokrouhlický, D., & Yokoyama, T. 2014, *AJ*, 148, 25
- Deienno, R., Walsh, K. J., Kretke, K. A., & Levison, H. F. 2019, *ApJ*, 876, 103
- Deienno, R., Walsh, K. J., Levison, H. F., & Kretke, K. A. 2020, *ApJ*, 890, 170
- Delbo, M. 2017, A 4 Gy-old Asteroid Family and the big void in the asteroid Main Belt, V1, Harvard Dataverse, doi:10.7910/DVN/MNA7QG
- Delbo, M., Avdellidou, C., & Morbidelli, A. 2019, *A&A*, 624, A69
- Delbo, M., Walsh, K., Bolin, B., Avdellidou, C., & Morbidelli, A. 2017, *Sci*, 357, 1026
- DeMeo, F. E., Binzel, R. P., Slivan, S. M., & Bus, S. J. 2009, *Icar*, 202, 160
- DeMeo, F. E., & Carry, B. 2013, *Icar*, 226, 723
- DeMeo, F. E., & Carry, B. 2014, *Natur*, 505, 629
- Drążkowska, J., & Dullemond, C. P. 2018, *A&A*, 614, A62
- Durda, D. D., Bottke, W. F., Nesvorný, D., et al. 2007, *Icar*, 186, 498
- Fraser, W. C., Brown, M. E., Morbidelli, A., Parker, A., & Batygin, K. 2014, *ApJ*, 782, 100
- Gradie, J., & Tedesco, E. 1982, *Sci*, 216, 1405
- Haisch, K. E. J., Lada, E. A., & Lada, C. J. 2001, *ApJL*, 553, L153
- Hansen, B. M. S. 2009, *ApJ*, 703, 1131
- Hayashi, C. 1981, *PThPS*, 70, 35
- Hayashi, C., Nakazawa, K., & Nakagawa, Y. 1985, in *Protostars and Planets II*, ed. D. C. Black & M. S. Matthews (Tucson, AZ: Univ. Arizona Press), 1100
- Hellmann, J. L., Schneider, J. M., Wölfer, E., et al. 2023, *ApJL*, 946, L34
- Huang, J., Andrews, S. M., Pérez, L. M., et al. 2018, *ApJL*, 869, L43
- Izidoro, A., Bitsch, B., Raymond, S. N., et al. 2021, *A&A*, 650, A152
- Izidoro, A., Dasgupta, R., Raymond, S. N., et al. 2022, *NatAs*, 6, 357
- Izidoro, A., Raymond, S. N., Morbidelli, A., & Winter, O. C. 2015, *MNRAS*, 453, 3619
- Izidoro, A., Raymond, S. N., Pierens, A., et al. 2016, *ApJ*, 833, 40
- Johansen, A., Ida, S., & Brasser, R. 2019, *A&A*, 622, A202
- Johansen, A., & Lambrechts, M. 2017, *AREPS*, 45, 359
- Johansen, A., Mac Low, M.-M., Lacerda, P., & Bizzarro, M. 2015, *SciA*, 1, 1500109
- Johansen, A., Ronnet, T., Bizzarro, M., et al. 2021, *SciA*, 7, eabc0444
- Johnson, B. C., Walsh, K. J., Minton, D. A., Krot, A. N., & Levison, H. F. 2016, *SciA*, 2, e1601658

- Kerridge, J. F. 1985, *Geochim. Cosmochim. Acta*, **49**, 1707
- Kretke, K. A., & Levison, H. F. 2014, *AJ*, **148**, 109
- Krot, A. N., Amelin, Y., Cassen, P., & Meibom, A. 2005, *Natur*, **436**, 989
- Kruijter, T. S., Burkhardt, C., Budde, G., & Kleine, T. 2017, *PNAS*, **114**, 6712
- Kruijter, T. S., Kleine, T., & Borg, L. E. 2020, *NatAs*, **4**, 32
- Laskar, J. 1997, *A&A*, **317**, L75
- Levison, H. F., Duncan, M. J., & Thommes, E. 2012, *AJ*, **144**, 119
- Levison, H. F., Kretke, K. A., & Duncan, M. J. 2015a, *Natur*, **524**, 322
- Levison, H. F., Kretke, K. A., Walsh, K. J., & Bottke, W. F. 2015b, *PNAS*, **112**, 14180
- Lichtenberg, T., Drazkowska, J., Schönbächler, M., Golabek, G. J., & Hands, T. O. 2021, *Sci*, **371**, 365
- Liu, B., Raymond, S. N., & Jacobson, S. A. 2022, *Natur*, **604**, 643
- Lykawka, P. S., & Ito, T. 2023, *NatSR*, **13**, 4708
- Michel, P., Benz, W., Tanga, P., & Richardson, D. C. 2001, *Sci*, **294**, 1696
- Minton, D. A., & Malhotra, R. 2010, *Icar*, **207**, 744
- Morbidelli, A., Baillié, K., Batygin, K., et al. 2022, *NatAs*, **6**, 72
- Morbidelli, A., Bottke, W. F., Nesvorný, D., & Levison, H. F. 2009, *Icar*, **204**, 558
- Morbidelli, A., Brasser, R., Gomes, R., Levison, H. F., & Tsiganis, K. 2010, *AJ*, **140**, 1391
- Mothé-Diniz, T., Carvano, J. M., & Lazzaro, D. 2003, *Icar*, **162**, 10
- Nakamura, T., Noguchi, T., Tanaka, M., et al. 2011, *Sci*, **333**, 1113
- Nanne, J. A. M., Nimmo, F., Cuzzi, J. N., & Kleine, T. 2019, *E&PSL*, **511**, 44
- Nelson, R. P. 2018, in *Handbook of Exoplanets*, ed. H. J. Deeg & J. A. Belmonte (Cham: Springer), 139
- Nesvorný, D. 2015a, *AJ*, **150**, 73
- Nesvorný, D. 2015b, *AJ*, **150**, 68
- Nesvorný, D. 2018, *ARA&A*, **56**, 137
- Nesvorný, D., Brož, M., & Carruba, V. 2015, in *Asteroids IV*, ed. P. Michel, F. E. DeMeo, & W. F. Bottke (Tucson, AZ: Univ. Arizona Press), 297
- Nesvorný, D., Dauphas, N., Vokrouhlický, D., Deianno, R., & Hopp, T. 2024, *E&PSL*, **626**, 118521
- Nesvorný, D., & Morbidelli, A. 2012, *AJ*, **144**, 117
- Nesvorný, D., Roig, F., & Bottke, W. F. 2017, *AJ*, **153**, 103
- Nesvorný, D., Roig, F. V., & Deianno, R. 2021, *AJ*, **161**, 50
- Nesvorný, D., Vokrouhlický, D., Bottke, W. F., & Levison, H. F. 2018, *NatAs*, **2**, 878
- O'Brien, D. P., Morbidelli, A., & Bottke, W. F. 2007, *Icar*, **191**, 434
- Pape, J., Mezger, K., Bouvier, A. S., & Baumgartner, L. P. 2019, *GeCoA*, **244**, 416
- Pierens, A., & Raymond, S. N. 2011, *A&A*, **533**, A131
- Pierens, A., Raymond, S. N., Nesvorný, D., & Morbidelli, A. 2014, *ApJL*, **795**, L11
- Raymond, S. N., & Izidoro, A. 2017a, *Icar*, **297**, 134
- Raymond, S. N., & Izidoro, A. 2017b, *SciA*, **3**, e1701138
- Raymond, S. N., Quinn, T., & Lunine, J. I. 2006, *Icar*, **183**, 265
- Ribeiro de Sousa, R., Morbidelli, A., Gomes, R., et al. 2022, *Icar*, **379**, 114933
- Robert, F., Merlivat, L., & Javoy, M. 1977, *Metic*, **12**, 349
- Roig, F., & Nesvorný, D. 2015, *AJ*, **150**, 186
- Simon, J. B., Armitage, P. J., Li, R., & Youdin, A. N. 2016, *ApJ*, **822**, 55
- Spitzer, F., Burkhardt, C., Budde, G., et al. 2020, *ApJL*, **898**, L2
- Troianskyi, V., Kankiewicz, P., & Oszkiewicz, D. 2023, *A&A*, **672**, A97
- Voelkel, O., Deianno, R., Kretke, K., & Klahr, H. 2021a, *A&A*, **645**, A131
- Voelkel, O., Deianno, R., Kretke, K., & Klahr, H. 2021b, *A&A*, **645**, A132
- Walsh, K. J., & Levison, H. F. 2016, *AJ*, **152**, 68
- Walsh, K. J., & Levison, H. F. 2019, *Icar*, **329**, 88
- Walsh, K. J., Morbidelli, A., Raymond, S. N., O'Brien, D. P., & Mandell, A. M. 2011, *Natur*, **475**, 206
- Walsh, K. J., Morbidelli, A., Raymond, S. N., O'Brien, D. P., & Mandell, A. M. 2012, *M&PS*, **47**, 1941
- Warren, P. H. 2011, *E&PSL*, **311**, 93
- Weidenschilling, S. J. 1977, *MNRAS*, **180**, 57
- Weiss, B. P., Bai, X.-N., & Fu, R. R. 2021, *SciA*, **7**, eaba5967
- Wetherill, G. W. 1980, *ARA&A*, **18**, 77
- Woo, J. M. Y., Morbidelli, A., Grimm, S. L., Stadel, J., & Brasser, R. 2023, *Icar*, **396**, 115497
- Zhu, M.-H., Morbidelli, A., Neumann, W., et al. 2021, *NatAs*, **5**, 1286